

Energy-stress-mediated AMPK activation inhibits ferroptosis

Hyemin Lee^{1,11}, Fereshteh Zandkarimi^{2,11}, Yilei Zhang¹, Jitendra Kumar Meena³, Jongchan Kim^{1,4}, Li Zhuang¹, Siddhartha Tyagi³, Li Ma^{1,5}, Thomas F. Westbrook^{3,6,7}, Gregory R. Steinberg⁸, Daisuke Nakada⁶, Brent R. Stockwell^{2,9*} and Boyi Gan^{1,5,10*}

Energy stress depletes ATP and induces cell death. Here we identify an unexpected inhibitory role of energy stress on ferroptosis, a form of regulated cell death induced by iron-dependent lipid peroxidation. We found that ferroptotic cell death and lipid peroxidation can be inhibited by treatments that induce or mimic energy stress. Inactivation of AMP-activated protein kinase (AMPK), a sensor of cellular energy status, largely abolishes the protective effects of energy stress on ferroptosis in vitro and on ferroptosis-associated renal ischaemia-reperfusion injury in vivo. Cancer cells with high basal AMPK activation are resistant to ferroptosis and AMPK inactivation sensitizes these cells to ferroptosis. Functional and lipidomic analyses further link AMPK regulation of ferroptosis to AMPK-mediated phosphorylation of acetyl-CoA carboxylase and polyunsaturated fatty acid biosynthesis. Our study demonstrates that energy stress inhibits ferroptosis partly through AMPK and reveals an unexpected coupling between ferroptosis and AMPK-mediated energy-stress signalling.

Normal cells require an adequate supply of nutrients and energy to survive. The depletion of nutrients and energy induces metabolic stress¹. One type of metabolic stress is energy stress, which is characterized by the depletion of intracellular ATP and a corresponding increase in intracellular AMP levels. Energy stress initially induces adaptive responses, which attempt to re-establish energy homeostasis. One important energy-stress-induced adaptive response is mediated by AMP-activated protein kinase (AMPK), a critical sensor of cellular energy status². In response to energy stress, AMPK is activated via AMP binding, upstream kinase phosphorylation and other mechanisms². Once activated, AMPK phosphorylates a myriad of downstream targets to promote ATP-generating catabolic processes and inhibit ATP-consuming anabolic processes, thereby restoring the energy balance and maintaining cell survival under conditions of energy stress³. However, under long-term and severe energy stress with excessive ATP depletion, such adaptive responses are unable to restore the energy balance and unresolved energy stress eventually induces apoptosis^{1,4,5}. Whether energy stress regulates other nonapoptotic forms of regulated cell death remains largely unknown.

Ferroptosis is a nonapoptotic form of regulated cell death that is induced by the overproduction of phospholipid hydroperoxides in an iron-dependent manner^{6–10}. Ferroptotic cell death is not associated with apoptotic hallmarks such as caspase-3 cleavage, can be induced in *BAX/BAK*-deficient cells and is suppressed by different inhibitors from those that block apoptosis or necroptosis; thus, ferroptosis is distinct from other forms of regulated cell death⁶. Dysregulation of ferroptosis is associated with various pathological

conditions and human diseases, such as ischaemia–reperfusion injury (IRI), neurodegeneration and cancer^{10–16}.

Accumulating evidence indicates an intimate link between metabolism and ferroptosis^{10,17}. The antioxidant enzyme glutathione peroxidase 4 (GPX4) uses reduced glutathione to convert phospholipid hydroperoxides to lipid alcohols and inhibits ferroptosis^{18,19}. Reduced glutathione is synthesized from glutamate, cysteine and glycine, among which cysteine is the rate-limiting precursor. Many cancer cells obtain cysteine mainly through the cystine–glutamate antiporter known as system x_c^- -mediated transport of extracellular cystine, which is an oxidized dimeric form of cysteine^{10,20}. Correspondingly, cystine depletion, inhibition of system x_c^- -mediated cystine transport by erastin or inactivation of GPX4 by RSL3 induces ferroptosis^{6,18}. How other metabolic processes or other forms of metabolic stress regulate ferroptosis remains less well understood. In this study, we uncover a hitherto unrecognized coupling between energy stress and ferroptosis, with implications for the treatment of ferroptosis-associated diseases.

Results

Energy stress inhibits ferroptotic cell death. Glucose provides the major energy source in most cells and glucose starvation depletes ATP and induces energy stress. To study the role of energy stress in ferroptosis, we first examined the effect of glucose starvation on erastin-induced ferroptosis in immortalized mouse embryonic fibroblasts (MEFs). As expected, erastin treatment did not induce hallmarks of apoptosis, such as caspase-3 or poly(ADP-ribose) polymerase (PARP) cleavage (Extended Data Fig. 1a), and

¹Department of Experimental Radiation Oncology, The University of Texas MD Anderson Cancer Center, Houston, TX, USA. ²Department of Biological Sciences, Columbia University, New York, NY, USA. ³Verna & Marrs McLean Department of Biochemistry and Molecular Biology, Baylor College of Medicine, Houston, TX, USA. ⁴School of Natural Sciences, Department of Life Sciences, Sogang University, Seoul, Republic of Korea. ⁵The University of Texas MD Anderson Cancer Center UTHHealth Graduate School of Biomedical Sciences, Houston, TX, USA. ⁶Department of Molecular and Human Genetics, Baylor College of Medicine, Houston, TX, USA. ⁷Therapeutic Innovation Center (THINC), Baylor College of Medicine, Houston, TX, USA. ⁸Centre for Metabolism, Obesity and Diabetes Research, Department of Medicine and Biochemistry and Biomedical Sciences, McMaster University, Hamilton, Ontario, Canada. ⁹Department of Chemistry, Columbia University, New York, NY, USA. ¹⁰Department of Molecular and Cellular Oncology, The University of Texas MD Anderson Cancer Center, Houston, TX, USA. ¹¹These authors contributed equally: Hyemin Lee, Fereshteh Zandkarimi. *e-mail: bstockwell@columbia.edu; bgan@mdanderson.org

erastin-induced cell death could be fully rescued by the ferroptosis inhibitor ferrostatin-1, the iron chelator deferoxamine (DFO) or the antioxidant *N*-acetyl-cysteine (NAC), but not by the apoptosis inhibitor carbobenzoxy-valyl-alanyl-aspartyl-[*O*-methyl]-fluoromethylketone (Z-VAD-FMK) or the necroptosis inhibitor necrostatin-1s (Extended Data Fig. 1b). Since glucose starvation is associated with reactive oxygen species (ROS) induction^{21,22} and ferroptosis is driven by lipid peroxidation¹⁰, which is a type of ROS, we initially hypothesized that glucose starvation may potentiate erastin-induced ferroptosis. To our surprise, we observed that glucose starvation largely rescued erastin-induced ferroptosis in MEFs (Fig. 1a,b). Time course experiments (Extended Data Fig. 1c) revealed that erastin treatment induced almost complete cell death within 16–24 h in immortalized MEFs, at which time points glucose starvation did not induce obvious cell death and almost completely rescued erastin-induced ferroptosis. The results are more difficult to interpret at later time points (48–96 h) because glucose starvation alone also induced substantial cell death. Notably, glucose-starvation-induced cell death could not be blocked by ferrostatin-1 but was associated with caspase-3 cleavage (Extended Data Fig. 1c,d), suggesting that glucose starvation induced apoptosis but not ferroptosis in MEFs.

Ferroptosis can also be induced by cystine depletion (Extended Data Fig. 1e), GPX4 deletion or inactivation by its inhibitors, such as RSL3 (ref. 18). We found that ferroptosis induced by cystine depletion, RSL3 treatment or GPX4 deletion were all substantially mitigated by glucose starvation (Fig. 1c–e). These data also suggested that glucose starvation probably impinges on the ferroptosis pathway downstream of GPX4, although we cannot completely rule out the possibility that glucose starvation might inhibit ferroptosis in parallel to or upstream of GPX4.

Further analysis in MEFs cultured in different concentrations of glucose revealed that ATP depletion correlated with the rescuing effects of glucose starvation on erastin-induced ferroptosis (Extended Data Fig. 1f,g). We further tested compounds that either induce or mimic energy stress, including 2-deoxy-D-glucose (2DG; a glucose analogue that blocks glycolysis), 5-aminoimidazole-4-carboxamide ribonucleotide (AICAR; an AMP analogue) and A769662 (an AMPK activator). While treatment with these compounds alone did not induce substantial cell death in immortalized MEFs, at least at the chosen concentrations and time frames, they all substantially inhibited lipid peroxidation and ferroptosis induced by erastin, cystine depletion or RSL3 treatment (Fig. 1f–k). We confirmed these findings in other cell lines, including Caki-1 and BJ cells (Extended Data Fig. 1h–k). Together, our results show that energy stress inhibits ferroptosis.

Energy stress inhibits ferroptotic cell death partly through AMPK. As all these treatments activate AMPK (Extended Data Fig. 1l), we tested whether AMPK is involved in energy-stress-mediated ferroptosis inhibition. Notably, *AMPK* double knockout (DKO) in MEFs almost completely reversed the inhibitory effect of glucose starvation, A769662 and 2DG on erastin-induced ferroptosis (Fig. 2a–c). It is known that defective AMPK signalling promotes energy-stress-induced cell death in MEFs^{23–25}. There was no obvious cell death in *AMPK* DKO MEFs cultured in glucose-free medium or treated with A769662 or 2DG at the time points when erastin induced potent ferroptosis (Fig. 2b,c). However, at the time point when erastin induced obvious ferroptosis, there was also substantial AICAR-induced cell death in *AMPK* DKO MEFs (Extended Data Fig. 1m), thus preventing us from examining the effect of *AMPK* deletion on AICAR-mediated ferroptosis inhibition. Notably, under treatment with 2 μ M erastin, we did not observe any difference in erastin-induced ferroptosis between *AMPK* wild-type (WT) and DKO MEFs (Fig. 2b,c), probably because basal AMPK phosphorylation levels are low in MEFs (Fig. 2d); therefore, energy stress is

needed to boost AMPK activity to reveal ferroptosis sensitivity differences between *AMPK* WT and DKO MEFs. Further dose-dependent analyses revealed that *AMPK* deletion promoted ferroptosis induced by low-dose erastin (0.25, 0.5 and 1 μ M) in MEFs (Extended Data Fig. 1n).

We further correlated basal AMPK activation status (*AMPK* T172 phosphorylation under 25 mM glucose) with ferroptosis sensitivity in a panel of cell lines. We also examined Solute Carrier Family 7 Member 11 (*SLC7A11*) expression levels in these cell lines (*SLC7A11* encodes xCT, which is a critical component of system x_c⁻²⁰). Such analyses revealed that all *SLC7A11*-high cells were relatively more resistant to ferroptosis compared with *SLC7A11*-low cells (Fig. 2d–h). Notably, while AMPK activation status did not correlate with ferroptosis sensitivity in *SLC7A11*-high cells, we observed an inverse correlation between AMPK activation and ferroptosis sensitivity in *SLC7A11*-low cells (Fig. 2d–h). Together, these data suggest that energy stress inhibits ferroptosis at least partly through AMPK.

AMPK inactivation sensitizes cancer cells to ferroptotic cell death. Our aforementioned data prompted us to further examine whether AMPK plays a causal role in ferroptosis resistance in the cell lines with high basal AMPK phosphorylation levels. We showed that inactivating AMPK using compound C dramatically sensitized ACHN cells (a ferroptosis-resistant cell line with high basal AMPK phosphorylation) to ferroptosis induced by erastin or cystine depletion (Fig. 3a,b; Extended Data Fig. 2a). Transmission electron microscopy (TEM) revealed that ACHN cells treated with compound C and erastin (or cystine depletion) exhibited shrunken mitochondria with increased membrane density, but did not show obvious DNA fragmentation in the nucleus, which is a characteristic morphologic feature of ferroptosis (Fig. 3c).

Overexpression of constitutively active (CA) AMPK (amino acids 1–312 of AMPK α 1) in Caki-1 cells (a ferroptosis-sensitive cell line with low basal AMPK activation) moderately increased ACC phosphorylation and partially protected cells from erastin-induced cell death (Fig. 3d,e). Conversely, *AMPK α 1/2* DKO in ACHN cells using CRISPR–Cas9 technology massively sensitized ACHN cells to ferroptosis induced by erastin, cystine depletion or RSL3 (Fig. 3f–k; Extended Data Fig. 2b). We further showed that re-expression of AMPK α 1, but not its T172A mutant or AMPK α 2, in *AMPK* DKO ACHN cells restored AMPK and ACC phosphorylation (Fig. 3l) and largely rescued increased ferroptosis sensitivity in *AMPK* DKO cells (Fig. 3m), suggesting that AMPK α 1 plays a dominant role in regulating ferroptosis in ACHN cells and that AMPK inhibits ferroptosis in a kinase-dependent manner. We subsequently confirmed our results in RCC4 cells, another ferroptosis-resistant cell line with high basal AMPK phosphorylation (Extended Data Fig. 2c–l). Finally, we showed that deletion of *LKB1*, the major upstream kinase of AMPK, also sensitized ACHN cells to ferroptosis (Extended Data Fig. 3a,b). Collectively, these results suggest that AMPK inhibits ferroptosis in cells with high basal AMPK activation.

AMPK-mediated ACC phosphorylation inhibits ferroptosis. We next sought to study the underlying mechanism(s) by which energy-stress-mediated AMPK activation regulates ferroptosis. In response to energy stress, AMPK activates catabolic processes, particularly autophagy, and inactivates anabolic processes, most notably fatty acid synthesis and protein synthesis². Since recent studies showed that autophagy promotes ferroptosis^{26,27}, but our results show that energy-stress-mediated AMPK activation inhibits ferroptosis, it is less likely that AMPK inhibits ferroptosis through its activation of autophagy. AMPK inhibits protein synthesis through its inhibition of mechanistic target of rapamycin complex 1 (mTORC1)²³. However, rapamycin treatment abolished mTORC1 activation (Extended Data Fig. 3c) but did not obviously affect erastin-induced

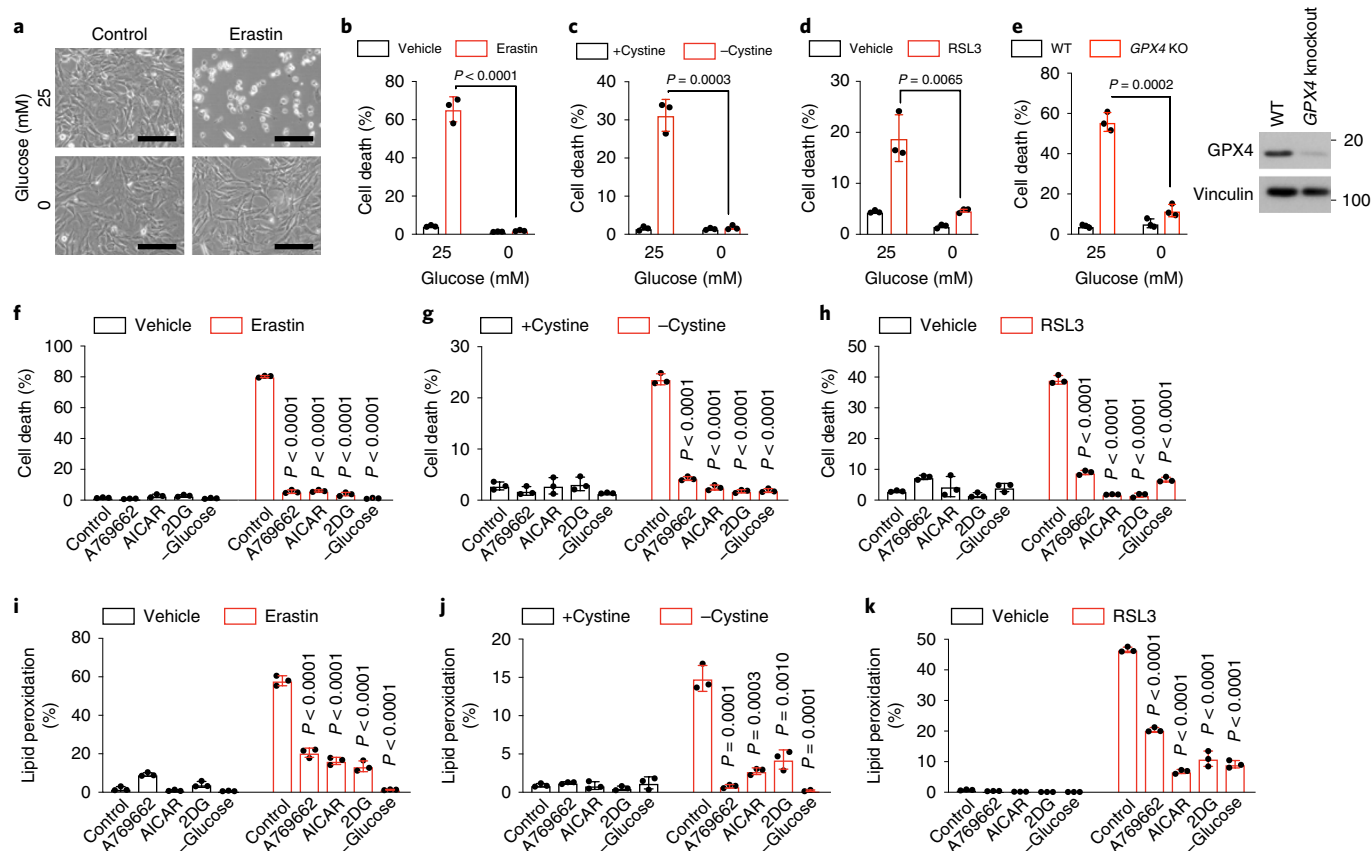


Fig. 1 | Energy stress inhibits ferroptotic cell death. **a**, Representative images showing the induction of cell death in immortalized MEFs treated with 2 μ M erastin cultured in 25 or 0 mM glucose for 16 h. Scale bars, 100 μ m. **b–d**, Cell death measurements in MEFs cultured in 25 or 0 mM glucose and treated with 2 μ M erastin for 16 h (**b**), cultured in cystine-free media for 8 h (**c**) or treated with 100 nM RSL3 for 16 h (**d**). **e**, Cell death measurement in *GPX4* WT and knockout Caki-1 cells cultured in 25 or 0 mM glucose for 16 h (left) and an immunoblot showing the levels of *GPX4* (right, values in kDa). **f–h**, Cell death measurements in MEFs treated with energy-stress inducer/mimetic agents including A769662 (200 μ M), AICAR (2 mM), 2DG (5 mM) and 0 mM glucose, with simultaneous treatments of 2 μ M erastin for 16 h (**f**), cystine-free media for 8 h (**g**) or 100 nM RSL3 for 16 h (**h**). **i–k**, Lipid peroxidation in MEFs treated with energy-stress inducer/mimetic agents and 2 μ M erastin for 8 h (**i**), cystine-free media for 6 h (**j**) or 100 nM RSL3 for 8 h (**k**). The *P* values correspond to the comparison between the control (red) and each treatment (red). The mean \pm s.d. are shown; *n* = 3 independent experiments. Statistical analysis was performed using an unpaired, two-tailed *t* test. Numerical source data and scanned images of unprocessed blots are provided as source data.

ferroptosis (Extended Data Fig. 3d), suggesting that AMPK probably regulates ferroptosis through mTORC1-independent mechanisms. In addition, AMPK deficiency or its activation by AICAR or 2DG treatment did not substantially affect cystine uptake (Extended Data Fig. 3e–g) or cellular iron levels (Extended Data Fig. 3h).

ACC1 and ACC2 are two related enzymes that catalyse the synthesis of malonyl-CoA from acetyl-CoA and function to promote fatty acid synthesis and inhibit fatty acid oxidation. Under energy stress, AMPK inhibits fatty acid synthesis through its phosphorylation and inhibition of both ACC1 and ACC2 (ref. ³). We found that, similar to glucose starvation, treatment with 5-(tetradecyloxy)-2-furoic acid (TOFA), an allosteric inhibitor of ACC (ref. ²⁸), potently inhibited lipid peroxidation (Fig. 4a–c) and ferroptosis (Fig. 4d–f; Extended Data Fig. 3i) induced by erastin, cystine depletion or RSL3 in MEFs. Similar observations were made in other cell lines (Extended Data Fig. 3j,k). Consistently, metabolite profiling confirmed that, similar to glucose starvation or AICAR treatment, TOFA treatment decreased the levels of various fatty acids such as palmitic acid (C16:0) (Extended Data Fig. 3l,m). Importantly, TOFA treatment substantially mitigated increased lipid peroxidation and ferroptosis sensitivity in *AMPK* DKO ACHN cells (Fig. 4g,h), suggesting that ACC is a key downstream effector of AMPK in the regulation of ferroptosis.

We next studied whether AMPK-mediated ACC phosphorylation plays a role in ferroptosis inhibition by energy stress. To this end, we generated MEFs from an *ACC* knock-in mouse model in which AMPK phosphorylation sites on both ACC1 (S79) and ACC2 (S212) were mutated to alanine (*ACC* double knock-in (DKI)) (Fig. 4j)^{29,30}. Similar to *AMPK* deficiency (Fig. 2a–c), mutation of AMPK phosphorylation sites on ACC largely blocked the inhibitory effect of A769662, AICAR or glucose starvation on erastin-induced ferroptosis (Fig. 4j–l). Together, our data strongly suggest that AMPK regulates ferroptosis at least partly through AMPK-mediated phosphorylation of ACC.

AMPK regulates polyunsaturated fatty acid (PUFA) generation.

The data above prompted us to characterize lipid profile alterations caused by AMPK activation or inactivation. To study the impact of AMPK activation on lipid metabolism, we performed untargeted lipidomic analyses in MEFs treated with vehicle (control), A769662, erastin or A769662 plus erastin (Extended Data Fig. 4a). As shown in Fig. 5a, A769662 treatment caused significant decreases (false discovery rate (FDR)-corrected *P* < 0.05; fold change > 1.5) in the levels of 64 lipid species compared with vehicle treatment. To examine the impact of AMPK deficiency on lipid metabolism, we also performed untargeted lipidomic analysis in *AMPK* WT and

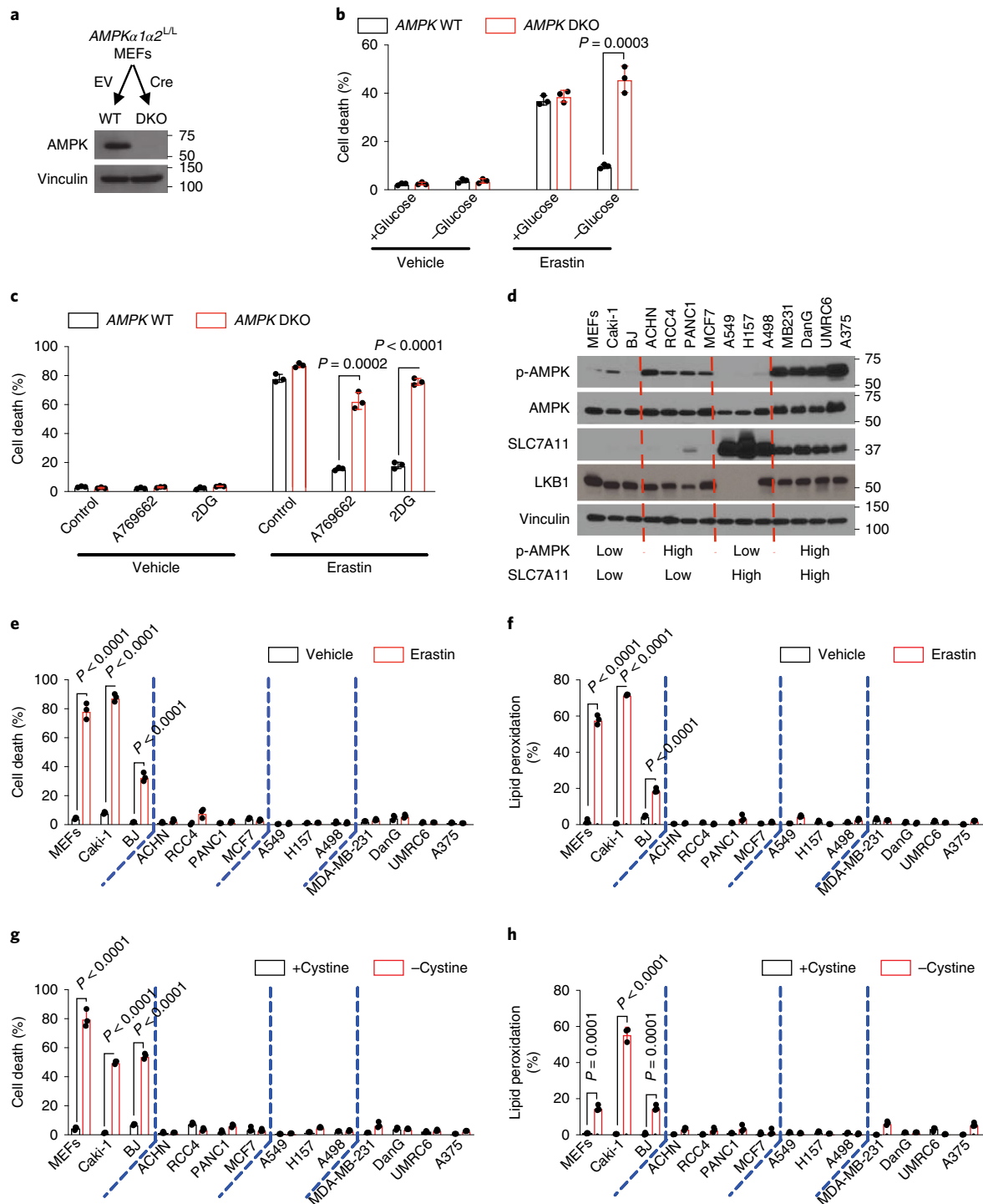


Fig. 2 | Energy stress inhibits ferroptotic cell death partly through AMPK. a, An immunoblot showing the levels of AMPK α in AMPK $\alpha 1\alpha 2$ WT and DKO MEFs. EV, empty vector; Cre, Cre recombinase. **b,c**, Cell death measurements in AMPK WT and DKO MEFs treated with erastin (2 μ M) cultured in 25 or 0 mM glucose for 16 h (**b**) or cotreated with A769662 (200 μ M) or 2DG (5 mM) for 16 h (**c**). **d**, An immunoblot showing the levels of AMPK T172 phosphorylation, AMPK, SLC7A11 and LKB1 in the cell lines indicated. P-AMPK, phospho-AMPK. **e**, Cell death measurement in the indicated cell lines at 24 h after 2 μ M erastin treatment. **f**, Lipid peroxidation measurement in the indicated cell lines treated with 2 μ M erastin for 24 h, except the MEFs (8 h), Caki-1 (16 h) and BJ (16 h) cell lines. **g,h**, The measurement of cell death (**g**) and lipid peroxidation (**h**) in the indicated cell lines cultured in cystine-free media for 36 and 16 h, respectively. Lipid peroxidation in MEFs was measured at 6 h. The mean \pm s.d. are shown; $n = 3$ independent experiments. Statistical analysis was performed using an unpaired, two-tailed t test. Numerical source data and scanned images of unprocessed blots are provided as source data. Dashed lines separate the cell line groups based on the levels of basal AMPK phosphorylation and SLC7A11 expression.

DKO ACHN cells with vehicle or erastin treatment (Extended Data Fig. 4b). As shown in Fig. 5b, we observed significant increases (FDR-corrected $P < 0.05$, fold change > 1.5) in the relative abundance

of 73 lipid species in AMPK DKO ACHN cells compared with WT ACHN cells (under vehicle treatment). Consistent with previous reports^{31,32}, erastin treatment altered the levels of several lipid species

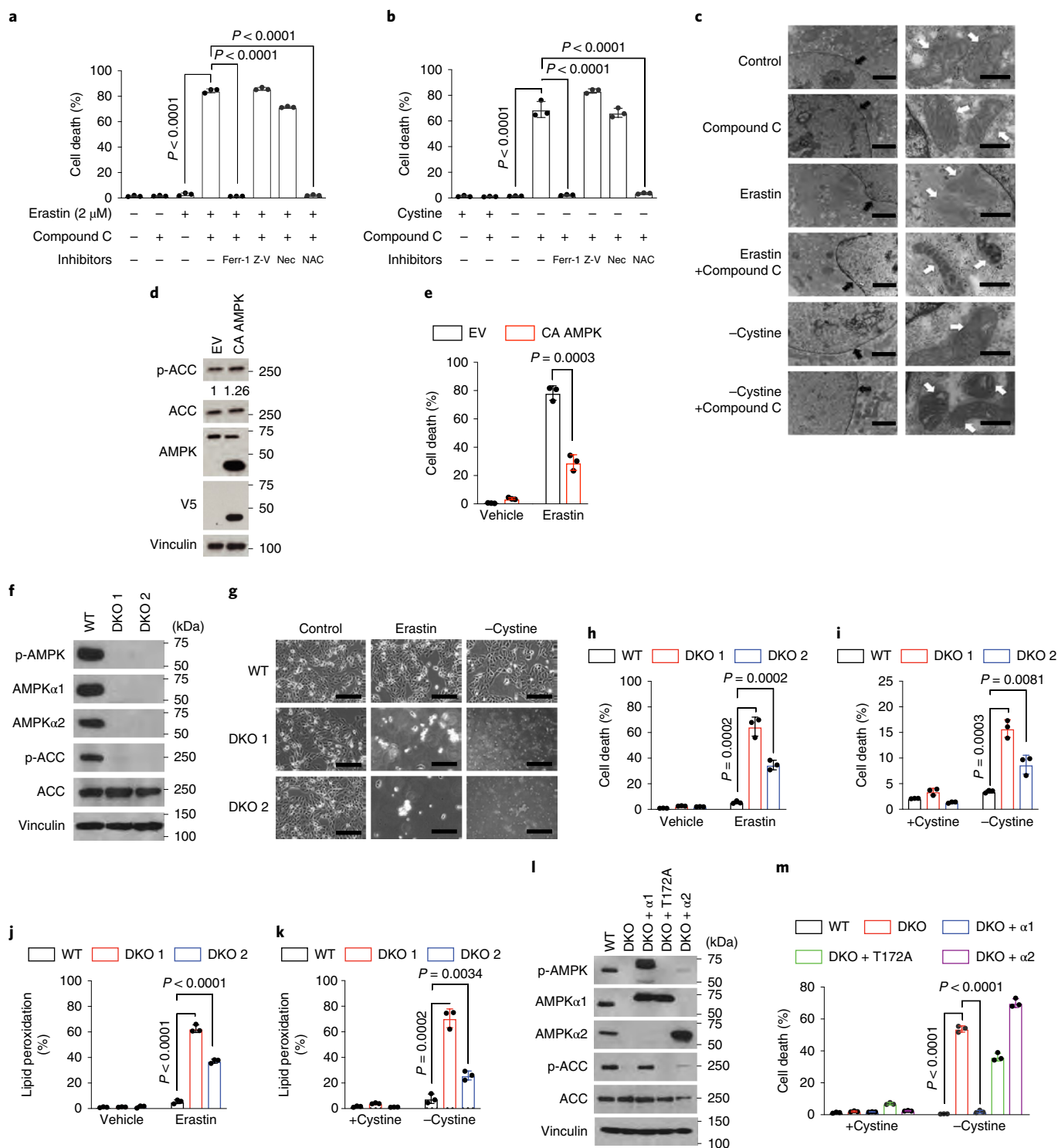


Fig. 3 | AMPK inactivation sensitizes cells to ferroptotic cell death. **a, b**, Cell death measurements in ACHN cells treated with AMPK inhibitor compound C, cell death inhibitors and 2 μ M erastin for 12 h (**a**) or in cystine-free media for 36 h (**b**). Ferr-1, 1 μ M ferrostatin-1; NAC, 5 mM; Nec, 2 μ M necrostatin-1s; Z-V, 20 μ M Z-VAD-FMK. **c**, TEM images of ACHN cells subjected to the indicated treatments for 9 h. Black arrows indicate nuclei; white arrows indicate mitochondria. Compound C, 10 μ M; control, vehicle; erastin, 2 μ M. Scale bars: left, 2 μ m; right, 500 nm. **d**, An immunoblot showing the expression of CA AMPK in Caki-1 cells. 1 and 1.26 represent the phospho-ACC to ACC ratio. EV, empty vector; p-ACC, phospho-ACC. **e**, Cell death measurement in Caki-1 cells expressing CA AMPK treated with 2 μ M erastin for 16 h. **f**, An immunoblot indicating the loss of AMPK α 1/ α 2 in AMPK DKO ACHN cell lines generated using the CRISPR-Cas9 system. **g**, Representative phase-contrast images showing cell death induced by 2 μ M erastin (24 h) or cystine withdrawal (36 h) in AMPK DKO ACHN cells. Scale bars, 100 μ m. **h, i**, Cell death measurements in AMPK WT and DKO ACHN cells treated with 2 μ M erastin for 18 h (**h**) or cultured in cystine-free media for 36 h (**i**). **j, k**, Lipid peroxidation measurements in AMPK WT and DKO ACHN cells treated with 2 μ M erastin for 12 h (**j**) or cultured in cystine-free media for 18 h (**k**). **l**, An immunoblot showing AMPK expression in ACHN cells as indicated. **m**, The measurement of cell death at 36 h post cystine withdrawal in ACHN cells as indicated. The mean \pm s.d. are shown; $n = 3$ independent experiments. Statistical analysis was performed using an unpaired, two-tailed t test. Numerical values and scanned images of unprocessed blots are provided as source data. In **d, f, i**, immunoblot values shown in kDa.

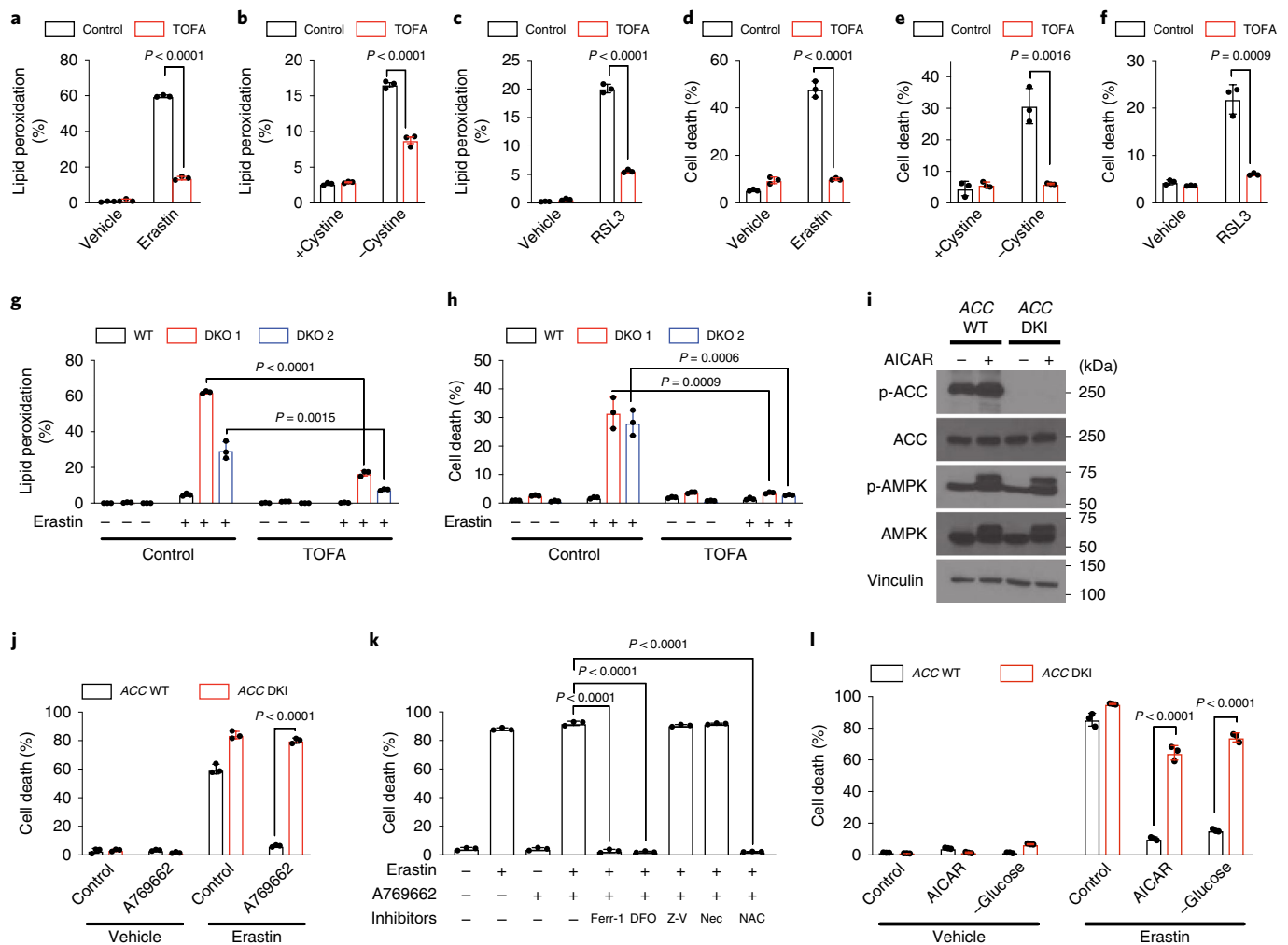


Fig. 4 | AMPK-mediated phosphorylation of ACC inhibits ferroptosis. a–c, Lipid peroxidation measurements in MEFs treated with or without 25 μ M TOFA and 2 μ M erastin for 8 h (**a**), cystine-free media for 6 h (**b**) or 100 nM RSL3 for 8 h (**c**). **d–f**, Cell death measurements in MEFs treated with or without 25 μ M TOFA and 2 μ M erastin for 16 h (**d**), cystine-free media for 8 h (**e**) or 100 nM RSL3 for 16 h (**f**). **g, h**, The measurement of lipid peroxidation (**g**) and cell death (**h**) in AMPK WT and DKO ACHN cells treated with 50 μ M TOFA and 2 μ M erastin for 12 h and 18 h, respectively. **i**, An immunoblot of ACC WT and ACC1 (S79A)/ACC2 (S212A) mutant DKI immortalized MEFs. **j**, Cell death measurement in ACC WT and DKI MEFs treated with 2 μ M erastin and 200 μ M A769662 for 16 h. **k**, Cell death measurement in ACC DKI MEFs treated with erastin, A769662 and various cell death inhibitors or NAC. DFO, 100 μ M; Ferr-1, 1 μ M ferrostatin-1; NAC, 5 mM; Nec, 2 μ M necrostatin-1; Z-V, 20 μ M Z-VAD-FMK. **l**, Cell death measurement in ACC WT and DKI MEFs treated with 2 μ M erastin and 2 mM AICAR or 0 mM glucose for 36 h. The mean \pm s.d. are shown; $n = 3$ independent experiments. Statistical analysis was performed using an unpaired, two-tailed *t* test. Numerical source data and scanned images of unprocessed blots are provided as source data.

in both analyses; importantly, A769662 treatment (or AMPK deletion) exerted similar global effects on lipid profiles under conditions of both vehicle and erastin treatment (Extended Data Fig. 4c,d).

By integrating the datasets from these two analyses, we identified 17 lipid species that were downregulated by A769662 treatment in MEFs but upregulated by AMPK deletion in ACHN cells (Fig. 5c and Extended Data Fig. 5a), including PUFAs such as dihomo- γ -linolenic acid (C20:3) and arachidonic acid (C20:4) (Fig. 5d,e). Further analyses confirmed that other fatty acids, such as palmitic acid (C16:0) and adrenic acid (C22:4), were similarly altered by AMPK activation or inactivation (although the fold changes did not meet the 1.5-fold cut-off under one or the other condition) (Extended Data Fig. 5b,c).

Accumulation of oxygenated phosphatidylethanolamines (PEs), specifically arachidonic acid (C20:4)- and adrenic acid (C22:4)-containing PEs, are believed to play direct roles in driving ferroptosis³³. Consistent with this, our lipidomic analyses showed that A769662 treatment decreased but AMPK deletion increased

the levels of PE 18:0_{20:4} and PE 18:0_{22:4} (Extended Data Fig. 6a,b). Acyl-CoA synthetase long chain family member 4 (ACSL4)-mediated PUFA-containing PE biosynthesis has been shown to be critical in driving ferroptosis^{31,33,34}. We showed that ACSL4 deletion largely blocked erastin-induced ferroptosis in AMPK DKO cells (Extended Data Fig. 6c,d). Supplementation of γ -linolenic acid (a precursor for dihomo- γ -linolenic acid synthesis) and arachidonic acid substantially sensitized A769662-treated MEFs or AMPK WT ACHN cells to erastin-induced ferroptosis (Fig. 5f,g). We confirmed that the supplementation of dihomo- γ -linolenic acid or arachidonic acid increased the levels of proferroptotic PE 18:0_{22:4} (and arachidonic acid treatment also increased the levels of PE 18:0_{20:4}) (Extended Data Fig. 6e,f). Finally, we showed that the supplementation of palmitic acid and stearic acid, the two most proximal fatty acids to AMPK, also sensitized ACHN cells to erastin-induced ferroptosis (Extended Data Fig. 6g,h).

To further substantiate our observations, we conducted untargeted lipidomic analysis in MEFs treated with TOFA (with or without

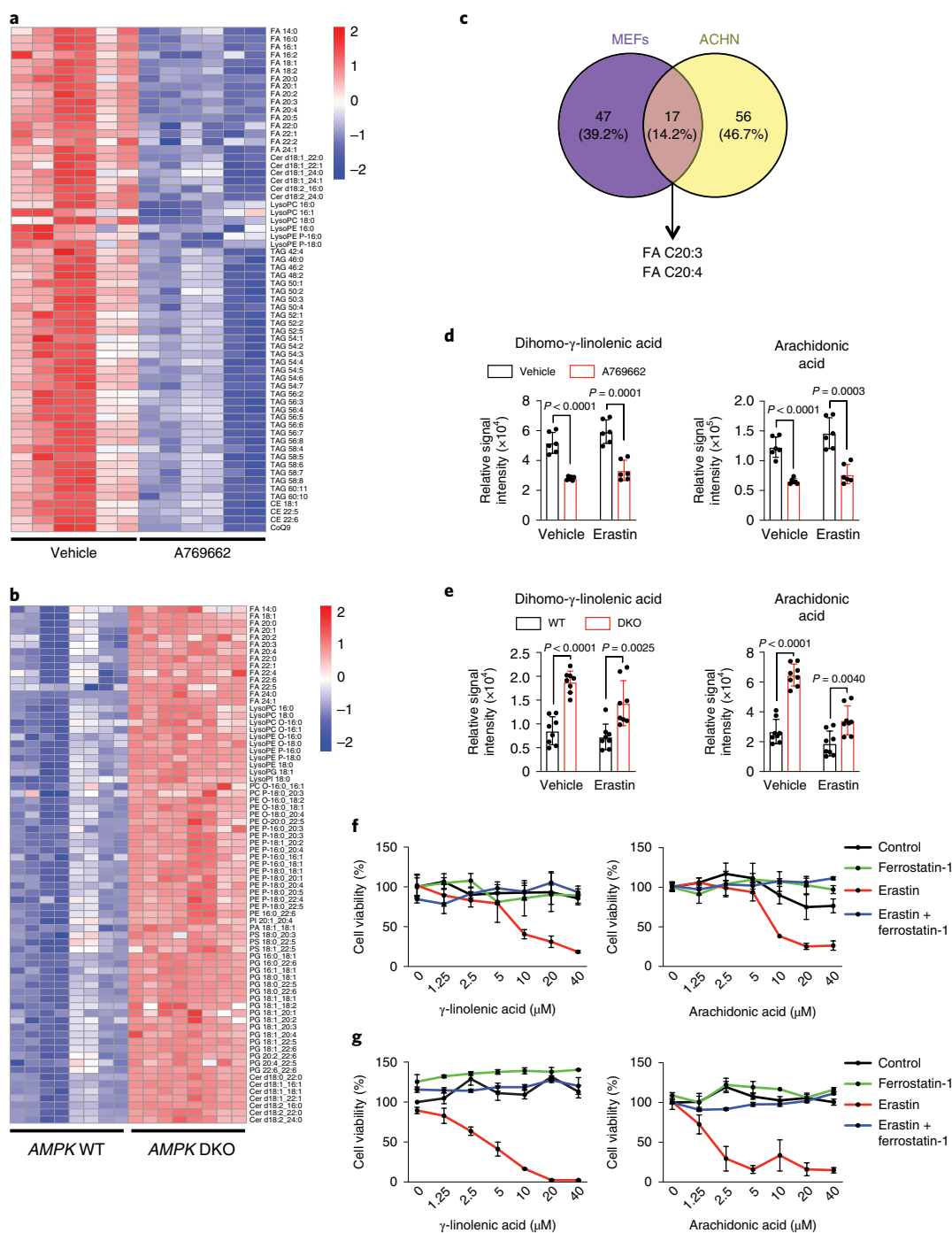


Fig. 5 | AMPK regulates PUFA-containing lipid accumulation. **a, b**, Heat maps of significantly changed lipid species (two-tailed, unpaired Welch's *t* test; fold-change threshold=1.5; FDR-corrected *P* < 0.05; *n* = 3 biologically independent samples) in vehicle- versus A769662-treated MEFs (**a**) and vehicle-treated AMPK WT versus DKO ACHN cells (**b**) measured in duplicates using UPLC-MS. Each row represents z-score-normalized intensities of the detected lipid species. Each column represents a sample. The relative abundance of each lipid is colour-coded, with red indicating high signal intensity and blue indicating low signal intensity. CE, cholesteryl ester; Cer, ceramide; CoQ9, coenzyme Q9; FA, free fatty acid; LysoPC, lysophosphatidylcholine; LysoPC O, ether-linked LysoPC; LysoPE, lysophosphatidylethanolamine; LysoPE O, ether-linked LysoPE; LysoPE P, plasmalogen LysoPE; LysoPG, lysophosphatidylglycerol; LysoPI, lysophosphatidylinositol; PA, phosphatidic acid; PC, phosphatidylcholine; PC O, ether-linked PC; PC P, plasmalogen PC; PE O, ether-linked PE; PE P, plasmalogen PE; PG, phosphatidylglycerol; PI, phosphatidylinositol; PS, phosphatidylserine; TAG, triacylglycerol. Lipids are annotated based on their fatty acyl compositions (for example, LysoPC 16:0 has 16 carbons and 0 double bonds) or as the sum of their total number of carbons and double bonds (for example, TAG 52:5 has a total of 52 carbons and 5 double bonds). **c**, A Venn diagram depicting the numbers of significantly altered lipids from the comparison of MEFs and ACHN cells. **d, e**, Relative signal intensities of dihomogamma-linolenic acid and arachidonic acid in MEFs (**d**) and ACHN cells (**e**) with the indicated treatments and genotypes. **f, g**, Cell viability measurements in MEFs treated with A769662 (**f**) or ACHN WT cells (**g**) incubated with the indicated fatty acids with a series of concentrations (0–40 μM) and treated with or without ferrostatin-1 or erastin as indicated. The mean ± s.d. are shown; *n* = 3 (**f, g**), *n* = 8 (**d**) or *n* = 8 (**e**) independent experiments. Statistical analysis was performed using an unpaired, two-tailed *t* test. Numerical source data are provided..

erastin treatment). We observed significant changes (one-way analysis of variance (ANOVA), FDR-corrected $P < 0.05$) in the relative abundance of many lipid species, including decreasing palmitic acid and palmitoleic acid levels, following TOFA treatment (Extended Data Fig. 6i,j). Notably, TOFA and A769662 treatments exhibited somewhat different lipidomic profiles (Extended Data Fig. 4c and Extended Data Fig. 6i). This is not entirely surprising, considering that AMPK activation by A769662 would also modulate other lipid metabolic enzymes besides inactivating ACC. Notably, A769662 and TOFA decreased the levels of the same PUFA-containing PEs, including PE 18:0_22:4, PE 18:1_22:6, PE 16:0_22:6, PE P-18:1_22:6, PE P-18:0_22:6 and triacylglycerols (Extended Data Fig. 7a–d), which is consistent with the current model in which it is the oxidation of PUFA-containing PEs that drives ferroptosis³³. Together, these lipidomic analyses suggest that AMPK activation suppresses and AMPK deficiency drives PUFA-containing lipid biosynthesis, thus altering cellular sensitivity to ferroptosis.

Energy-stress-induced AMPK activation inhibits renal IRI. Our findings from cell line studies prompted further analysis of AMPK function in ferroptosis-associated pathological conditions in vivo. Consistent with previous studies that indicated a role for ferroptosis in renal IRI^{13,19}, TEM analysis revealed a striking ferroptosis-associated morphologic change in renal epithelial cells following renal IRI characterized by smaller mitochondria with increased membrane density (Fig. 6a). To examine whether energy-stress inducers would protect from renal IRI by inhibiting ferroptosis, we treated WT mice with vehicle, AICAR, 2DG or ferrostatin-1 (as a positive control) and then subjected the mice to an established renal IRI protocol¹³. As expected, AICAR or 2DG treatment substantially increased AMPK phosphorylation in kidneys (Fig. 6b). Consistent with previous findings¹³, ferrostatin-1 treatment partially protected mice from renal IRI as quantified by tubular damage in the renal cortex (characterized by tubular dilatation, tubule brush border loss, flattened epithelial cells or sloughing of cells); notably, AICAR or 2DG treatment exhibited a similar protective effect on renal IRI as ferrostatin-1 did (Fig. 6c,d).

To study the potential role of AMPK in renal IRI, we generated the *AMPK α 1*/ α 2^{L/L}, *Rosa26-CreERT2* mouse model (hereafter referred to as AMPK DKO). Tamoxifen treatment substantially decreased AMPK levels in the kidneys of AMPK DKO mice compared with those in the *AMPK α 1*/ α 2^{L/L} control (hereafter referred to as AMPK WT) mice (Extended Data Fig. 8a). Consistent with a recent report using the same mouse model³⁵, AMPK DKO mice maintained a normal body weight for at least 2 months after tamoxifen treatment and did not show obvious phenotypic differences in their kidneys before or after IRI compared with WT controls (Extended Data Fig. 8b). Similar to our observations made in MEFs (see Fig. 2a–c), we found that the AICAR-mediated protective effect on renal IRI-induced renal damage and blood urea nitrogen (BUN) levels was largely abolished in AMPK DKO mice (Fig. 6e–g). Immunohistochemical analysis of 4-hydroxy-2-nonenal (4-HNE; a lipid peroxidation marker) revealed that 4-HNE staining substantially overlapped with tubular damage in the renal cortex following ischaemia reperfusion (Extended Data Fig. 8c). AMPK deletion did not affect IR-induced 4-HNE staining in kidneys in vehicle-treated mice but suppressed the protective effects of AICAR treatment to reduce 4-HNE staining (Fig. 6h,i). This observation was further confirmed with immunohistochemical analysis using malondialdehyde, another lipid peroxidation marker (Extended Data Fig. 8d,e). Together, these in vivo data strongly suggest that energy stress exerts a protective effect on renal IRI at least partly through AMPK activation, which potentially relates to an energy-stress-mediated inhibitory effect on lipid peroxidation and ferroptosis. It should be noted that a protective role of AMPK in the regulation of renal IRI has also been described in previous studies, possibly via

AMPK-mediated autophagy activation^{36,37}. Our study further suggests that AMPK may regulate renal IRI through ferroptosis.

Discussion

Glucose is the principal nutrient required to maintain biosynthetic, bioenergetic and redox homeostasis and to maintain cell survival in most cells³⁸. Glucose starvation leads to cell death due to ROS induction and/or energy depletion^{4,22}. As ferroptosis is induced by lipid peroxidation, a type of ROS-mediated lipid damage, it seems logical that, if anything, glucose starvation should promote ferroptosis. In this study, we revealed a counterintuitive finding that glucose is required for ferroptosis and that glucose starvation largely prevents cells from undergoing ferroptosis. We found that treatments that induce or mimic energy stress inhibit ferroptosis in vitro or ferroptosis-associated renal IRI in vivo at least partly through AMPK activation. Under these conditions with low basal AMPK activation, boosting AMPK activation by energy stress inhibits ferroptosis. Conversely, in ferroptosis-resistant cell lines with high basal AMPK activation, AMPK inactivation dramatically sensitizes these cells to ferroptosis. Collectively, our study convincingly establishes an inhibitory role of AMPK in regulating ferroptosis and further suggests that AMPK activators may be useful to treat the diseases or pathological conditions induced by ferroptosis, such as IRI. Mechanistically, our data suggest that the inhibitory effects of AMPK activation on ferroptosis do not involve the modulation of autophagy, mTORC1 signalling, cystine uptake or iron metabolism. Instead, our data support a model in which energy stress activates AMPK and AMPK then phosphorylates and inactivates ACC, resulting in the restrained biosynthesis of PUFAs and other fatty acids and ferroptosis inhibition (Extended Data Fig. 9).

A recent study showed that mitochondria play an important role in regulating ferroptosis³⁹. AMPK is also vital for the regulation of mitochondrial homeostasis⁴⁰. However, there is a major difference between mitochondria and AMPK function in ferroptosis. While mitochondria selectively promote cystine-starvation-induced or erastin-induced, but not RSL3-induced, ferroptosis³⁹, our data clearly show that glucose starvation or AMPK deficiency affects ferroptosis induced by all of these ferroptosis inducers. Therefore, our data suggest that energy-stress-mediated AMPK activation probably inhibits ferroptosis through mitochondria-independent mechanisms. Furthermore, since lipid metabolism, and particularly PUFA biosynthesis, is important for ferroptosis mediated by different ferroptosis inducers^{31,33,34}, our proposed model linking AMPK-mediated lipid metabolism to ferroptosis is in line with the data that AMPK deficiency sensitizes cells to all of the ferroptosis inducers that we have tested.

A recent study also reported a promoting role of AMPK in the regulation of ferroptosis⁴¹, which is opposite to our findings described here. There are several discrepancies between these studies. First, in contrast to this study, we did not observe any major effects of erastin on AMPK or ACC phosphorylation in the cell lines that we examined (Extended Data Fig. 2a). In addition, while this study proposed that AMPK-mediated Beclin 1 (BECN1) phosphorylation promotes ferroptosis by inhibiting SLC7A11-mediated cystine transport, we found that AMPK deletion or its activation by AICAR or 2DG treatment did not substantially affect cystine uptake (Extended Data Fig. 3e–g). It is possible that AMPK function in the regulation of ferroptosis is context dependent, and this awaits further investigation in future studies.

We and others previously showed that ferroptosis is also an important tumour suppression mechanism^{11,14,42–45}. Although ferroptosis has been linked to multiple pathological conditions or diseases, its physiological function still remains enigmatic. We propose that tumour suppression may represent one physiological function of this form of regulated cell death. Our current study linking AMPK to ferroptosis also raises an intriguing question regarding whether

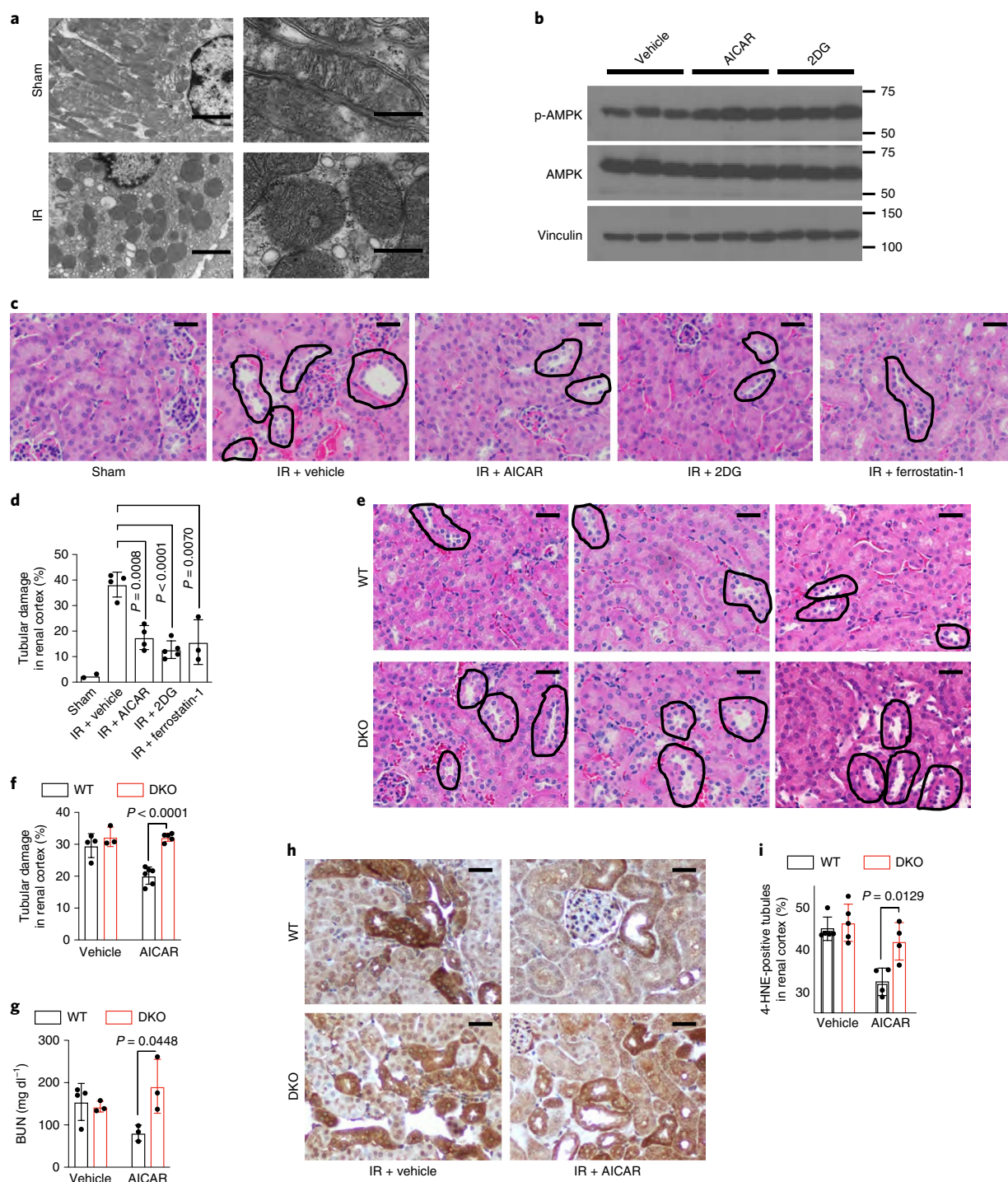


Fig. 6 | AMPK activation protects from renal IRI. a, TEM images of cortical renal tissues from mice after ischaemia reperfusion (IR) or sham treatment. Scale bars: left, 2 μm ; right, 500 nm. The experiment was repeated three times, independently, with similar results. **b–d**, WT mice injected with vehicle, AICAR (0.5 mg g^{-1}), 2DG (0.5 mg g^{-1}) or ferrostatin-1 ($2 \mu\text{g g}^{-1}$) were subjected to 30 min of IR. A western blot analysis showing AMPK activation in the tissue lysates from mouse kidneys (**b**); the experiment was repeated three times, independently, with similar results. Representative images of haematoxylin and eosin (H&E) staining of the renal cortex after IR (**c**); black lines show damaged renal proximal tubules (as characterized by tubular dilatation, tubule brush border loss, flattened epithelial cells or sloughing of cells); scale bars, 50 μm . Bar graphs showing the percentage tubular damage in the renal cortex (**d**); the mean \pm s.d. are shown; $n = 2$ (sham), $n = 3$ (IR + ferrostatin-1), $n = 4$ (IR + vehicle, IR + AICAR) or $n = 5$ (IR + 2DG) mice. **e–i**, AMPK WT and DKO mice injected with either vehicle or AICAR for 7 d were subjected to IR. Representative images of H&E staining showing the damaged renal cortex after IR plus AICAR (**e**); scale bars, 50 μm . Bar graphs showing the percentage tubular damage (**f**); the mean \pm s.d. are shown; $n = 3$ (DKO + vehicle), $n = 4$ (WT + vehicle), $n = 5$ (DKO + AICAR) or $n = 6$ (WT + AICAR) mice. Bar graphs showing BUN levels (**g**); the mean \pm s.d. are shown; $n = 3$ (DKO + vehicle, WT + AICAR, DKO + AICAR) or $n = 4$ (WT + vehicle) mice. Representative images showing 4-HNE immunohistochemical staining from mouse renal cortex with the indicated genotypes and treatment conditions (**h**); dark brown stained tubules indicate 4-HNE-positive staining; scale bars, 50 μm . Bar graphs showing the percentage of 4-HNE-positive tubules per visual field (**i**); the mean \pm s.d. are shown; $n = 4$ (AICAR) or 5 (vehicle). Statistical analysis was performed using an unpaired, two-tailed *t* test. Numerical source data and scanned images of unprocessed blots are provided as source data.

AMPK regulation of ferroptosis plays a role in tumour biology. The exact role of AMPK in tumour biology is highly context dependent. AMPK can exert either a tumour-suppressive function by inhibiting major biosynthetic pathways (such as protein or fatty acid biosynthesis) or a tumour-promoting function by promoting tumour cell survival under metabolic stress conditions⁴⁶. While the tumour-suppressive role of the AMPK pathway is well established⁴⁷, multiple recent studies have also convincingly established a tumour-promoting role of AMPK in some tumour types^{35,48–51}; in addition, some isoforms of AMPK are overexpressed or amplified in certain cancers⁵². In light of our current data showing that AMPK inhibits ferroptosis, it is tempting to speculate that AMPK's pro-tumorigenic function might be at least partly mediated through its inhibition of ferroptosis in some contexts. Future studies will further dissect the potential role of ferroptosis in AMPK-mediated tumour development.

Online content

Any methods, additional references, Nature Research reporting summaries, source data, extended data, supplementary information, acknowledgements, peer review information; details of author contributions and competing interests; and statements of data and code availability are available at <https://doi.org/10.1038/s41556-020-0461-8>.

Received: 28 May 2019; Accepted: 3 January 2020;
Published online: 6 February 2020

References

- Green, D. R., Galluzzi, L. & Kroemer, G. Cell biology. Metabolic control of cell death. *Science* **345**, 1250256 (2014).
- Hardie, D. G., Ross, F. A. & Hawley, S. A. AMPK: a nutrient and energy sensor that maintains energy homeostasis. *Nat. Rev. Mol. Cell Biol.* **13**, 251–262 (2012).
- Hardie, D. G., Schaffer, B. E. & Brunet, A. AMPK: an energy-sensing pathway with multiple inputs and outputs. *Trends Cell Biol.* **26**, 190–201 (2015).
- El Mjiyad, N., Caro-Maldonado, A., Ramirez-Peinado, S. & Munoz-Pinedo, C. Sugar-free approaches to cancer cell killing. *Oncogene* **30**, 253–264 (2011).
- Lin, A. et al. The FoxO-BNIP3 axis exerts a unique regulation of mTORC1 and cell survival under energy stress. *Oncogene* **33**, 3183–3194 (2014).
- Dixon, S. J. et al. Ferroptosis: an iron-dependent form of nonapoptotic cell death. *Cell* **149**, 1060–1072 (2012).
- Xie, Y. et al. Ferroptosis: process and function. *Cell Death Differ.* **23**, 369–379 (2016).
- Cao, J. Y. & Dixon, S. J. Mechanisms of ferroptosis. *Cell. Mol. Life Sci.* **73**, 2195–2209 (2016).
- Yang, W. S. & Stockwell, B. R. Ferroptosis: death by lipid peroxidation. *Trends Cell Biol.* **26**, 165–176 (2016).
- Stockwell, B. R. et al. Ferroptosis: a regulated cell death nexus linking metabolism, redox biology, and disease. *Cell* **171**, 273–285 (2017).
- Jiang, L. et al. Ferroptosis as a p53-mediated activity during tumour suppression. *Nature* **520**, 57–62 (2015).
- Gao, M., Monian, P., Quadri, N., Ramasamy, R. & Jiang, X. Glutaminolysis and transferrin regulate ferroptosis. *Mol. Cell* **59**, 298–308 (2015).
- Linkermann, A. et al. Synchronized renal tubular cell death involves ferroptosis. *Proc. Natl Acad. Sci. USA* **111**, 16836–16841 (2014).
- Zhang, Y. et al. BAP1 links metabolic regulation of ferroptosis to tumour suppression. *Nat. Cell Biol.* **20**, 1181–1192 (2018).
- Chen, L., Hambright, W. S., Na, R. & Ran, Q. Ablation of the ferroptosis inhibitor glutathione peroxidase 4 in neurons results in rapid motor neuron degeneration and paralysis. *J. Biol. Chem.* **290**, 28097–28106 (2015).
- Do Van, B. et al. Ferroptosis, a newly characterized form of cell death in Parkinson's disease that is regulated by PKC. *Neurobiol. Dis.* **94**, 169–178 (2016).
- Shimada, K. et al. Global survey of cell death mechanisms reveals metabolic regulation of ferroptosis. *Nat. Chem. Biol.* **12**, 497–503 (2016).
- Yang, W. S. et al. Regulation of ferroptotic cancer cell death by GPX4. *Cell* **156**, 317–331 (2014).
- Friedmann Angeli, J. P. et al. Inactivation of the ferroptosis regulator Gpx4 triggers acute renal failure in mice. *Nat. Cell Biol.* **16**, 1180–1191 (2014).
- Koppula, P., Zhang, Y., Zhuang, L. & Gan, B. Amino acid transporter SLC7A11/xCT at the crossroads of regulating redox homeostasis and nutrient dependency of cancer. *Cancer Commun.* **38**, 12 (2018).
- Dai, F. et al. BAP1 inhibits the ER stress gene regulatory network and modulates metabolic stress response. *Proc. Natl Acad. Sci. USA* **114**, 3192–3197 (2017).
- Hay, N. Reprogramming glucose metabolism in cancer: can it be exploited for cancer therapy? *Nat. Rev. Cancer* **16**, 635–649 (2016).
- Inoki, K., Zhu, T. & Guan, K. L. TSC2 mediates cellular energy response to control cell growth and survival. *Cell* **115**, 577–590 (2003).
- Shaw, R. J. et al. The tumor suppressor LKB1 kinase directly activates AMP-activated kinase and regulates apoptosis in response to energy stress. *Proc. Natl Acad. Sci. USA* **101**, 3329–3335 (2004).
- Liu, X. et al. LncRNA NBR2 engages a metabolic checkpoint by regulating AMPK under energy stress. *Nat. Cell Biol.* **18**, 431–442 (2016).
- Hou, W. et al. Autophagy promotes ferroptosis by degradation of ferritin. *Autophagy* **12**, 1425–1428 (2016).
- Gao, M. et al. Ferroptosis is an autophagic cell death process. *Cell Res.* **26**, 1021–1032 (2016).
- Bianchi, A., Evans, J. L., Nordlund, A. C., Watts, T. D. & Witters, L. A. Acetyl-CoA carboxylase in reuber hepatoma cells: variation in enzyme activity, insulin regulation, and cellular lipid content. *J. Cell. Biochem.* **48**, 86–97 (1992).
- Houde, V. P. et al. AMPK β 1 reduces tumor progression and improves survival in p53 null mice. *Mol. Oncol.* **11**, 1143–1155 (2017).
- Fullerton, M. D. et al. Single phosphorylation sites in Acc1 and Acc2 regulate lipid homeostasis and the insulin-sensitizing effects of metformin. *Nat. Med.* **19**, 1649–1654 (2013).
- Yang, W. S. et al. Peroxidation of polyunsaturated fatty acids by lipoxygenases drives ferroptosis. *Proc. Natl Acad. Sci. USA* **113**, E4966–E4975 (2016).
- Skouta, R. et al. Ferrostatins inhibit oxidative lipid damage and cell death in diverse disease models. *J. Am. Chem. Soc.* **136**, 4551–4556 (2014).
- Kagan, V. E. et al. Oxidized arachidonic and adrenic PEs navigate cells to ferroptosis. *Nat. Chem. Biol.* **13**, 81–90 (2017).
- Doll, S. et al. ACSL4 dictates ferroptosis sensitivity by shaping cellular lipid composition. *Nat. Chem. Biol.* **13**, 91–98 (2017).
- Chhipa, R. R. et al. AMP kinase promotes glioblastoma bioenergetics and tumour growth. *Nat. Cell Biol.* **20**, 823–835 (2018).
- Wang, L. T. et al. Protective role of AMP-activated protein kinase-evoked autophagy on an in vitro model of ischemia/reperfusion-induced renal tubular cell injury. *PLoS ONE* **8**, e79814 (2013).
- Decleves, A. E., Sharma, K. & Satriano, J. Beneficial effects of AMP-activated protein kinase agonists in kidney ischemia-reperfusion: autophagy and cellular stress markers. *Nephron Exp. Nephrol.* **128**, 98–110 (2014).
- Boroughs, L. K. & DeBerardinis, R. J. Metabolic pathways promoting cancer cell survival and growth. *Nat. Cell Biol.* **17**, 351–359 (2015).
- Gao, M. et al. Role of mitochondria in ferroptosis. *Mol. Cell* **73**, 354–363 (2019).
- Herzig, S. & Shaw, R. J. AMPK: guardian of metabolism and mitochondrial homeostasis. *Nat. Rev. Mol. Cell Biol.* **19**, 121–135 (2018).
- Song, X. et al. AMPK-mediated BECN1 phosphorylation promotes ferroptosis by directly blocking system X_c^- activity. *Curr. Biol.* **28**, 2388–2399 (2018).
- Zhang, Y., Zhuang, L. & Gan, B. BAP1 suppresses tumor development by inducing ferroptosis upon SLC7A11 repression. *Mol. Cell. Oncol.* **6**, 1536845 (2019).
- Liu, T., Jiang, L., Tavana, O. & Gu, W. The deubiquitylase OTUB1 mediates ferroptosis via stabilization of SLC7A11. *Cancer Res.* **79**, 1913–1924 (2019).
- Chu, B. et al. ALOX12 is required for p53-mediated tumour suppression through a distinct ferroptosis pathway. *Nat. Cell Biol.* **21**, 579–591 (2019).
- Gan, B. DUBbing ferroptosis in cancer cells. *Cancer Res.* **79**, 1749–1750 (2019).
- Hardie, D. G. Molecular pathways: is AMPK a friend or a foe in cancer? *Clin. Cancer Res.* **21**, 3836–3840 (2015).
- Shackelford, D. B. & Shaw, R. J. The LKB1–AMPK pathway: metabolism and growth control in tumour suppression. *Nat. Rev. Cancer* **9**, 563–575 (2009).
- Saito, Y., Chapple, R. H., Lin, A., Kitano, A. & Nakada, D. AMPK protects leukemia-initiating cells in myeloid leukemias from metabolic stress in the bone marrow. *Cell Stem Cell* **17**, 585–596 (2015).
- Kishton, R. J. et al. AMPK is essential to balance glycolysis and mitochondrial metabolism to control T-ALL cell stress and survival. *Cell Metab.* **23**, 649–662 (2016).
- Eichner, L. J. et al. Genetic analysis reveals AMPK is required to support tumor growth in murine Kras-dependent lung cancer models. *Cell Metab.* **29**, 285–302 (2018).
- Jeon, S. M., Chandel, N. S. & Hay, N. AMPK regulates NADPH homeostasis to promote tumour cell survival during energy stress. *Nature* **485**, 661–665 (2012).
- Ross, F. A., MacKintosh, C. & Hardie, D. G. AMP-activated protein kinase: a cellular energy sensor that comes in 12 flavours. *FEBS J.* **283**, 2987–3001 (2016).

Publisher's note Springer Nature remains neutral with regard to jurisdictional claims in published maps and institutional affiliations.

© The Author(s), under exclusive licence to Springer Nature Limited 2020

Methods

Mice. All animal experiments were performed in accordance with a protocol approved by the Institutional Animal Care and Use Committee (IACUC) of The University of Texas MD Anderson Cancer Center; the protocol is in full compliance with policies of the IACUC. *AMPKα1/α2^{+/L}* mice were provided by D. Nakada⁴⁸ and crossed with *Rosa26-CreERT2* mice as described in our previous publications^{53,54}. Five-week-old mice were intraperitoneally injected with tamoxifen (Sigma-Aldrich, 120 μg g⁻¹ body weight) for five consecutive days. Mice were subjected to IRI at two weeks post tamoxifen injection. For AICAR (Toronto Research Chemicals) or 2DG (Sigma-Aldrich) treatment, mice were either injected with vehicle (PBS) or drugs (0.5 mg g⁻¹) at 10 d after the last tamoxifen injection for 7 d. IRI was performed on the following day. Ferrostatin-1 (Sigma-Aldrich) was injected 30 min before IRI. All mouse injections were intraperitoneal and the doses were calculated according to mouse body weight.

Primary cells. Primary MEFs were established from embryos at E13.5 as previously described⁵⁵. MEFs were cultured in Dulbecco's modified Eagle's medium (DMEM) with 10% fetal bovine serum (FBS) and 1% penicillin/streptomycin at 37 °C in an incubator with a humidified atmosphere of 20% O₂ and 5% CO₂. The primary MEFs were immortalized by infection with SV40 large T antigen (LT-MEFs). To generate *AMPKα1/α2* WT and DKO MEFs, *AMPKα1/α2^{+/L}* LT-MEFs were infected with either an empty vector control (pBABE-EV) or Cre-recombinase-expressing retrovirus (pBABE-Cre) and selected with puromycin (2 μg ml⁻¹) for 4 d. Immortalized ACC WT and DKI MEFs were previously described²⁹.

Cancer cell lines. BJ, ACHN, Caki-1, A498, MCF7, MDA-MB-231, A375 and A549 cell lines were obtained from the American Type Culture Collection (ATCC). RCC4 and UMR6 cell lines were obtained from W. G. Kaelin at the Dana-Farber Cancer Institute. PANC-1 and DanG cell lines were obtained from H. Ying at the MD Anderson Cancer Center. The H157 cell line was obtained from J. A. Roth at the MD Anderson Cancer Center. All cell lines were cultured in culture media supplemented with 10% (volume/volume; v/v) FBS and 1% (v/v) penicillin/streptomycin at 37 °C in an incubator with a humidified atmosphere of 20% O₂ and 5% CO₂. RCC4, PANC-1, A549, MDA-MB-231, DanG, UMR6 and A375 cell lines were cultured in DMEM (Sigma, D6429). BJ, ACHN, MCF7 and A498 cell lines were cultured in Eagle's Minimum Essential Medium (ATCC, 30-2003). The H157 cell line was cultured in RPMI-1640 medium (Sigma, R8758) and the Caki-1 cell line was cultured in McCoy's 5a Medium Modified (ATCC, 30-2007).

All cell lines were cultured in a 10-cm plate and subcultured into a 12-well plate for cell death and lipid peroxidation measurement. For cell viability assays, cells were subcultured into a 96-well plate. Cells were treated with ferroptosis inducers, erastin (EMD Millipore) or RSL3 (Selleckchem); apoptosis inducer, staurosporine (LC Laboratories); cell death inhibitors, ferrostatin-1 (Sigma-Aldrich), necrostatin-1s (BioVision) or Z-VAD-FMK (R&D Systems); antioxidant, NAC (Sigma-Aldrich); iron chelator, DFO (Sigma-Aldrich); AMPK activator/inhibitors, A769662 (LC Laboratories), AICAR (Toronto Research Chemicals), 2DG (Sigma-Aldrich), compound C (Sigma-Aldrich); ACC inhibitor, TOFA (Millipore). For glucose-free media and cystine-free media treatment, cells were cultured in normal growth media and then subcultured into 12-well plates. After overnight culture, cells were washed twice with PBS and the media was replaced with glucose- or cystine-free media. Dialysed FBS was used for glucose-free and cystine-free media.

Plasmid constructs. The gateway donor vectors containing the AMPKα1 WT and T172A mutant were described in our previous publications^{25,56}. These genes were integrated into the pLenti6.3/V5 destination vector (Invitrogen) using gateway cloning. The sequences were verified from single clones. The pLenti-CMV/TO_PRKAA2 (AMPKα2) was obtained from Addgene (plasmid no. 74447). The CA AMPK construct was described in our previous publication²⁵.

CRISPR-Cas9-mediated gene knockout. Knockout of *AMPKα1/α2*, *LKB1*, *GPX4* and *ACSL4* in human cell lines was performed using single guide RNAs (sgRNAs) and CRISPR-Cas9 technology. sgRNAs were cloned into the lentiviral lentiCRISPR v2 vector or transient expression vector, pSpCas9(BB)-2A-GFP (PX458). sgAMPKα1: CCAGGAAGTGA GTCTGCGCA, CTCACCTTCACTTGGCCGA, TACTC AATCGACAGAAGATT; sgAMPKα2: GAAGATCGGACTACTGTCG, GTTGGAGAAC ATCAATTAAC, ACTTACAGTTTGATAATATG; sgLKB1: CCCTGGTCCAGCATGGA GG, CACGGAGGGCGAGCTGATGT, AGCTTGGCCGCTTGGCGCG; sgGPX4: GAG ATCAAAGAGTTCGCCG; sgACSL4: AATAAAGCAGAGTACCCTGA, GAAGCGGTT GGTCTACTTGG. lentiCRISPR v2 clones were transfected into HEK293T cells with psPAX2 packaging plasmid and pMD2.G VSV-G envelope expressing plasmid. ACHN cells were infected with lentivirus with 0.8 μg ml⁻¹ of polybrene, selected with puromycin (2 μg ml⁻¹, Invivogen) for 3 d and then single cells were sorted into 96-well plates. For the transient transfection of PX458-guide RNA clones, an SF Cell Line 4D-Nucleofector X kit (Lonza) was used according to the manufacturer's protocol. Briefly, 2 × 10⁵ ACHN cells mixed with 1 μg of plasmid, nucleofector solution and supplement were subjected to nucleofection using a 4D-Nucleofector core unit. 24 h after the transfection, GFP-positive

single cells were sorted into 96-well plates. Single cells were maintained in Eagle's Minimum Essential Medium (ATCC, 30-2003) with 10% (v/v) FBS and 1% (v/v) penicillin/streptomycin at 37 °C in an incubator with 5% CO₂ for 3–4 weeks and each colony was verified by western blot and DNA sequencing to confirm the target gene deletion. To enhance the gene silencing efficiency, we also used the construct with doxycycline (DOX)-inducible Cas9 expression, which was kindly provided by T.F. Westbrook (Baylor College of Medicine). ACHN cells were infected with lentivirus carrying DOX-inducible Cas9 and selected with 400 μg ml⁻¹ G418 (Sigma-Aldrich). 1 μg ml⁻¹ of DOX (Sigma-Aldrich) was added to the media 48 h before PX458-guide RNA infection and cells were then cultured in DOX-free media 24 h after the sgRNA infection.

To generate *GPX4* knockout cells, DOX-inducible Cas9 expressing Caki-1 cells were infected with sgRNAs targeting *GPX4*. DOX was added to the media in the presence of 1 μM ferrostatin-1. Cells were cultured with standard cell culture media supplemented with 1 μM ferrostatin-1. To induce ferroptosis, ferrostatin-1 was removed from the media.

Cell death assays. Cell death was measured by propidium iodide (Roche) staining using a flow cytometer, as previously described^{57,58}. For propidium iodide-staining, cells were seeded at a density of 70–80% confluence into 12-well plates. The next day, cells were treated with different reagents and media. To measure cell death, the cells were collected (including floating dead cells), stained with 5 μg ml⁻¹ propidium iodide and the percentage of the propidium iodide-positive dead cell population was analysed using the flow cytometer BD Accuri C6 (BD Biosciences) and an FL2 detector. A minimum of 5,000 single cells were analysed per well and all experiments were carried out at least in triplicate. For cells treated simultaneously with ferroptosis inducers and energy-stress inducers, appropriate times were selected to analyse cell death/lipid peroxidation before the lethal effect of energy-stress inducers.

Cell viability assay. Viable cells were measured using Cell Counting Kit-8 (CCK-8, Dojindo), as previously described^{59,60}. Briefly, ACHN cells were seeded onto 96-well plates at a density of 2 × 10⁴ per well. The next day, cells were treated with fatty acids for 24 h. Subsequently, cells were treated with erastin or left untreated for 16 h and then exposed to 10 μl of CCK-8 reagent (100 μl medium per well) for 1 h at 37 °C, 5% CO₂ in an incubator. The absorbance at a wavelength of 450 nm was determined using a FLUOstar Omega microplate reader (BMG Labtech).

Determination of lipid peroxidation. Cells were seeded on 12-well plates and incubated overnight. The next day, cells were treated with compounds for the indicated times, harvested by trypsinization and resuspended in 200 μl PBS containing 5 μM C11-BODIPY 581/591 (Invitrogen). Cells were incubated for 30 min at 37 °C in a water bath. Lipid peroxidation was assessed using the flow cytometer BD Accuri C6 with a 488 nm laser on an FL1 detector. A minimum of 5,000 single cells were analysed per well.

Intracellular ATP level measurement. Intracellular ATP levels were measured using a CellTiter-Glo Luminescent assay kit (Promega, G7570) according to the manufacturer's instructions and as previously described⁶¹. Briefly, 10,000 cells per well were seeded in a 96-well plate 1 d before treatment. After the cells were cultured in media with different glucose concentrations, as indicated, each well received 100 μl CellTiter-Glo Reagent before incubation for 10 min at room temperature on a shaker. The luminescence of each well was subsequently measured with a Gen5 microplate reader (BIOTEK).

Fatty acid-dependent sensitization of ferroptosis. MEFs and ACHN cells were plated onto 96-well plates at a density of 1 × 10⁴ per well (MEFs) and 2 × 10⁴ per well (ACHN). After overnight incubation, cells were treated with specified fatty acids or fatty acids + 1 μM ferrostatin-1 with a series of fatty acid concentrations ranging from 40 to 0 μM for 24 h. Subsequently, cells were treated simultaneously with fatty acids with or without 2 μM erastin for 12 h (MEFs) or 18 h (ACHN) and cell viability was evaluated using CCK-8 reagent.

Cystine uptake assay. The cystine uptake assay was conducted as previously described¹⁴. Briefly, cells were plated in 12-well plates and incubated overnight. To measure the cystine uptake, the medium was replaced with fresh DMEM (which contains 200 μM cystine) containing [¹⁴C] cystine (PerkinElmer, 0.04 μCi) and the cells were incubated for 2 or 4 h. For Extended Data Fig. 3f,g, cells were pretreated with AICAR or 2DG for 4 h and [¹⁴C] cystine was added into the media for an additional 2 h. The uptake was terminated by rapidly rinsing cells twice with cold PBS and lysing in 0.1 mM NaOH. Radioactivity (disintegrations per minute) was measured using a Tri-Carb Liquid Scintillation Analyzer (PerkinElmer, 4810TR) in the presence of a quench curve. All experiments were carried out in triplicate.

Labile iron pool measurement. ACHN cells were seeded into 12-well plates at a density of 2 × 10⁵ per well. On the following day, cells were incubated with 20 nM calcein-AM (C3099, Invitrogen) for 15 min and washed with PBS. Cells were then harvested and analysed using the flow cytometer BD Accuri C6 with a 488 nm laser on an FL1 detector.

Immunoblotting. Western blotting to analyse protein expression was performed as previously described^{62–64}. Briefly, cell pellets and tissues were lysed using RIPA lysis buffer (Millipore) and the protein concentration was determined by a Bradford assay (Bio-Rad) using a Nanodrop2000 (Thermo scientific). 15–20 µg of protein was used for immunoblot analysis using antibodies against phospho-AMPKα (T172, 1:1,000, 2535, Cell Signaling), AMPKα (1:1,000, 5832, Cell Signaling), AMPKα1 (1:1,000, 2795, Cell Signaling), AMPKα2 (1:1,000, 2757, Cell Signaling), phospho-ACC (S79, 1:1,000, 3661, Cell Signaling), ACC (1:1,000, 3662, Cell Signaling), phospho-S6 (S240/244, 1:5,000, 3661, Cell Signaling), S6 (1:1,000, 2217, Cell Signaling), phospho-S6K (T389, 1:1,000, 9205, Cell Signaling), S6K (1:1,000, sc-230, Santa Cruz), phospho-ULK1 (S757, 1:1,000, 6888, Cell Signaling), ULK1 (1:1,000, 8054, Cell Signaling), LKB1 (1:1,000, sc-32245, Santa Cruz), SLC7A11 (1:3,000, 12691, Cell Signaling), GPX4 (1:1,000, MAB5457, R&D systems), ACSL4 (1:1,000, sc-271800, Santa Cruz), cleaved caspase-3 (D175, 1:500, 9661, Cell Signaling), cleaved-PARP (D214, 1:1,000, 9544, Cell Signaling) and vinculin (1:50,000, V4505, Sigma).

Histology, analysis of organ damage and immunohistochemistry. Fresh kidney tissues were fixed in 10% neutral buffered formalin overnight, washed once with PBS and stored in 70% ethanol at 4°C. The tissues were dehydrated and embedded in paraffin by the Research Histology Core Laboratory (MD Anderson Cancer Center) according to standard protocols. Embedded tissues were sectioned at a thickness of 5 µm for H&E, 4-HNE and MDA staining. H&E-stained kidney sections were analysed using an Olympus BX43 microscope. Organ damage on the renal cortex was evaluated using the following parameters: tubular dilatation, tubule brush border loss, flattened epithelial cells and sloughing of cells. The primary antibodies, 4-HNE (ab46545, Abcam, 1:200) or MDA (JAI-MMD-030N, Adipogen, 1:100), were incubated overnight at 4°C. Staining was performed using the Vectastain elite ABC kit and DAB peroxidase substrate kit (Vector laboratories). Images were randomly taken from the renal cortex (ten images per mouse) at ×200 magnification using an Olympus BX43 microscope and the percentage of 4-HNE-positive tubular cells per image was analysed.

Kidney IRI. Induction of kidney IRI was performed via the dorsal approach and bilateral renal pedicle clamping for 30 min. Mice were anaesthetized with an intraperitoneal injection of ketamine (100 mg kg⁻¹, Henry Schein)/ xylazine (10 mg kg⁻¹, Sigma) and an analgesic, sustained-release buprenorphine (ZooPharm), was injected subcutaneously. Throughout the surgical procedure, heating pads were used to maintain mouse body temperature. Via the dorsal approach, the right kidney was removed and the left renal pedicle was clamped for 30 min using a vascular clamp. The muscle layer and skin layer were closed using 5-0 vicryl sutures (Ethicon). Sham-operated mice underwent identical surgical procedures, except the renal pedicle clamping. All mice were killed 24 h after reperfusion. In some experiments, AICAR (0.5 mg g⁻¹) and 2DG (0.5 mg g⁻¹) were injected into mice 7 d before IRI and the surgical procedure was performed on the day following the last AICAR/2DG injection. For ferostatin-1 treatment, mice were injected with 200 µl of PBS for 7 d and 2 µg g⁻¹ of ferostatin-1 was injected into the mice 30 min before ischaemia. For the TEM analysis, fresh kidneys were cut into slices perpendicular to the long axis from the renal cortex and 1 mm³ cubes were fixed at 4°C using the solution provided by the High Resolution Electron Microscopy Facility at the MD Anderson Cancer Center.

TEM. TEM analysis was performed by the High Resolution Electron Microscopy facility at the MD Anderson Cancer Center. Samples were fixed with a solution containing 3% glutaraldehyde plus 2% paraformaldehyde in 0.1 M cacodylate buffer, pH 7.3, then washed in 0.1 M sodium cacodylate buffer and treated with 0.1% Millipore-filtered cacodylate-buffered tannic acid, postfixed with 1% buffered osmium and stained en bloc with 1% Millipore-filtered uranyl acetate. The samples were dehydrated in increasing concentrations of ethanol, infiltrated and embedded in LX-112 medium. The samples were polymerized in a 60°C oven for approximately 3 d. Ultrathin sections were cut in a Leica Ultracut microtome (Leica), stained with uranyl acetate and lead citrate in a Leica EM Stainer and examined in a JEM 1010 transmission electron microscope (JEOL, USA, Inc.) at an accelerating voltage of 80 kV. Digital images were obtained using the AMT Imaging System (Advanced Microscopy Techniques Corp.).

Lipidomic analyses. Sample preparation. Lipids were extracted from each cell pellet using a modified Matyash⁶⁵ method, as described previously⁶⁶. Briefly, MEFs were cultured in 0 mM glucose-containing media or treated with vehicle (DMSO), 2 mM AICAR, 200 µM A769662, 25 µM TOFA, 2 µM erastin, 200 µM A769662 + 2 µM erastin or 25 µM TOFA + 2 µM erastin for 8 h. AMPK WT and DKO ACHN cells were treated with vehicle (DMSO) or 2 µM erastin for 11 h. In addition, ACHN cells were treated with vehicle (DMSO), 20 µM dihomo-γ-linolenic acid or 20 µM arachidonic acid for 18 h. For Extended Data Fig. 3m, the frozen cell pellets were processed and analysed by the Mayo Clinic Hospital metabolomics core. All the other lipidomic analyses were performed as follows. Cells were homogenized in 250 µl cold methanol containing 0.01% butylated hydroxytoluene and 1 µl of SPLASH lipidomics internal standard mix (Avanti Polar Lipids, Inc.)

with a microtip solicitor. Homogenized samples were transferred to fresh glass vials containing 850 µl of cold methyl-tert-butyl ether (MTBE) and vortex-mixed for 30 s. To enhance the lipid extraction efficiency, the samples were incubated on ice for 2 h on the shaker. After the addition of 200 µl of ice-cold water, the samples were incubated for 20 min on ice and centrifuged at 3,000 r.p.m. for 20 min at 4°C. The upper phase containing the lipids was collected and dried down under a gentle stream of nitrogen gas. The dried samples were reconstituted with 2-propanol/acetonitrile/water (4:3:1, v/v/v) and 0.01% butylated hydroxytoluene before LC-MS analysis. A quality control sample was prepared by combining 40 µl of each sample to assess the reproducibility of the features through the runs.

LC conditions. Lipids were separated using an Acquity UPLC HSS T3 column (2.1 × 100 mm, 1.8 µm) over a 17-min gradient elution on a Waters Acquity UPLC I-Class system. Mobile phase A consisted of acetonitrile/water (60:40, v/v) and mobile phase B was 2-propanol/acetonitrile/water (85:10:5, v/v/v) both containing 10 mM ammonium acetate and 0.1% acetic acid. The gradient profile was 40% B for 1.5 min, 40–100% B in 10.5 min, 100% B for 3 min, 40% B in 1 min and 40% B for 1 min. The oven temperature was set at 55°C and the flow rate was 400 µl min⁻¹. The injection volume was 6 µl using the flow-through needle mode. The quality control sample was injected between the samples and at the beginning and end of the run to monitor the performance and the stability of the MS platform.

MS conditions. The SYNAPT G2-Q-ToF mass spectrometer was operated in both positive and negative electrospray ionization modes. For the positive mode, a capillary voltage and sampling cone voltage of 3 kV and 32 V were used. The source and desolvation temperatures were kept at 120 and 500°C, respectively. Nitrogen was used as the desolvation gas with a flow rate of 900 l h⁻¹. For the negative mode, a capillary voltage of 2 kV and a cone voltage of 30 V were used. The source temperature was 120°C and the desolvation gas flow was set to 850 l h⁻¹. Depending on the ionization mode, the protonated molecular ion of leucine encephalin ([M + H]⁺, mass to charge ratio (*m/z*): 556.2771) or the deprotonated molecular ion ([M - H]⁻, *m/z*: 554.2615) was used as a lock mass for mass accuracy and reproducibility. The data were collected in duplicates in data-independent (MS^E) mode over the mass range *m/z*: 50 to 1,600 Da. The quality control sample was also acquired in enhanced data-independent ion mobility (HDMSE) in both positive and negative modes for enhancing the structural assignment of lipid species. The electrospray ionization source settings for ion mobility were the same as described above. The travelling wave velocity was set to 650 m s⁻¹ and the wave height was 40 V. The helium gas flow in the helium cell region of the ion-mobility spectrometry cell was set to 180 ml min⁻¹. Nitrogen, used as the drift gas, was held at a flow rate of 90 ml min⁻¹ in the ion-mobility spectrometry cell. The low collision energy was set to 4 eV and the high collision energy was ramped from 25 to 65 eV in the transfer region of the T-Wave device to induce the fragmentation of mobility-separated precursor ions.

Data preprocessing and statistical analysis. All raw data files were converted to netCDF format using the DataBridge tool implemented in MassLynx software (Waters, version 4.1). Then, the data were subjected to peak-picking, retention time alignment and grouping using the XCMS (refs. 67,68) package (version 3.0.2) in an R (version 3.4.4) environment. After retention time alignment and filling missing peaks, an output data frame was generated including the list of time-aligned detected lipid features (*m/z* and retention time) and the relative signal intensity (area of the chromatographic peak) in each sample. Multivariate and univariate statistical analyses were performed using MetaboAnalyst⁶⁹ (version 4.0) and also in an R environment. Group differences were calculated using either a two-tailed parametric Welch's *t* test with a fold-change threshold of 1.5 (average signal intensities of treated over average signal intensities of vehicle groups) or one-way ANOVA. *P* values were corrected for multiple hypothesis testing and a FDR of 0.05 or less was considered significant.

Structural assignment of identified lipids. The structural elucidation and validation of significant features were initially obtained by searching monoisotopic masses against the available online databases, such as METLIN⁷⁰, Lipid MAPS⁷¹ and HMDB⁷² with a mass tolerance of 5 ppm. Fragment ion information obtained by tandem MS (UPLC-HDMSE) was used for the further structural elucidation of significantly changed lipid species. HDMSE data were processed using MS^E data viewer (version 1.3, Waters Corp.).

Statistics and reproducibility. All experiments were independently repeated more than two times with similar results. The statistical analyses (unpaired, two-tailed *t* test) shown in bar plots were performed with GraphPad Prism 8 software using a two-tailed Student's *t* test, unless otherwise mentioned. The data are presented as means ± s.d. of three biologically independent experiments or samples. For the lipidomics analysis in Extended Data Fig. 4c,d, one-way ANOVA was performed. A *P* value less than 0.05 was considered significant.

Reporting Summary. Further information on research design is available in the Nature Research Reporting Summary linked to this article.

Data availability

The mass spectrometry raw data files and metadata have been deposited in the EMBL-EBI MetaboLights database with the identifier [MTBLS1399](https://www.ebi.ac.uk/metabolights/MTBLS1399). All data supporting the findings of this study are available from the corresponding author on reasonable request. Source data for Figs. 1–6 and Extended Data Figs. 1–3 and 5–8 are presented with the paper.

References

- Gan, B. et al. mTORC1-dependent and -independent regulation of stem cell renewal, differentiation, and mobilization. *Proc. Natl Acad. Sci. USA* **105**, 19384–19389 (2008).
- Gan, B. et al. FoxOs enforce a progression checkpoint to constrain mTORC1-activated renal tumorigenesis. *Cancer Cell* **18**, 472–484 (2010).
- Lee, H. et al. BAF180 regulates cellular senescence and hematopoietic stem cell homeostasis through p21. *Oncotarget* **7**, 19134–19146 (2016).
- Chauhan, A. S. et al. STIM2 interacts with AMPK and regulates calcium-induced AMPK activation. *FASEB J.* **33**, 2957–2970 (2019).
- Xiao, Z. D. et al. Energy stress-induced lncRNA *FILNC1* represses c-Myc-mediated energy metabolism and inhibits renal tumor development. *Nat. Commun.* **8**, 783 (2017).
- Liu, X. & Gan, B. lncRNA *NBR2* modulates cancer cell sensitivity to phenformin through GLUT1. *Cell Cycle* **15**, 3471–3481 (2016).
- Koppula, P., Zhang, Y., Shi, J., Li, W. & Gan, B. The glutamate/cystine antiporter SLC7A11/xCT enhances cancer cell dependency on glucose by exporting glutamate. *J. Biol. Chem.* **292**, 14240–14249 (2017).
- Zhang, Y., Koppula, P. & Gan, B. Regulation of H2A ubiquitination and SLC7A11 expression by BAP1 and PRC1. *Cell Cycle* **11** (2019).
- Gan, B. et al. Lkb1 regulates quiescence and metabolic homeostasis of haematopoietic stem cells. *Nature* **468**, 701–704 (2010).
- Lin, A. et al. FoxO transcription factors promote AKT Ser473 phosphorylation and renal tumor growth in response to pharmacological inhibition of the PI3K–AKT pathway. *Cancer Res.* **74**, 1682–1693 (2014).
- Gan, B., Yoo, Y. & Guan, J. L. Association of focal adhesion kinase with tuberous sclerosis complex 2 in the regulation of s6 kinase activation and cell growth. *J. Biol. Chem.* **281**, 37321–37329 (2006).
- Gan, B., Melkounian, Z. K., Wu, X., Guan, K. L. & Guan, J. L. Identification of FIP200 interaction with the TSC1–TSC2 complex and its role in regulation of cell size control. *J. Cell Biol.* **170**, 379–389 (2005).
- Matyash, V., Liebisch, G., Kurzchalia, T. V., Shevchenko, A. & Schwudke, D. Lipid extraction by methyl-tert-butyl ether for high-throughput lipidomics. *J. Lipid Res.* **49**, 1137–1146 (2008).
- Zhang, Y. et al. Imidazole ketone erastin induces ferroptosis and slows tumor growth in a mouse lymphoma model. *Cell Chem. Biol.* **26**, 623–633 (2019).
- Smith, C. A., Want, E. J., O'Maille, G., Abagyan, R. & Siuzdak, G. XCMS: processing mass spectrometry data for metabolite profiling using nonlinear peak alignment, matching, and identification. *Anal. Chem.* **78**, 779–787 (2006).
- Tautenhahn, R., Bottcher, C. & Neumann, S. Highly sensitive feature detection for high resolution LC/MS. *BMC Bioinformatics* **9**, 504 (2008).
- Chong, J. et al. MetaboAnalyst 4.0: towards more transparent and integrative metabolomics analysis. *Nucleic Acids Res.* **46**, W486–W494 (2018).
- Montenegro-Burke, J. R., Guigas, C. & Siuzdak, G. METLIN: a tandem mass spectral library of standards. *Methods Mol. Biol.* **2104**, 149–163 (2020).
- Fahy, E. et al. Update of the LIPID MAPS comprehensive classification system for lipids. *J. Lipid Res.* **50**, S9–S14 (2009).
- Wishart, D. S. et al. HMDB 4.0: the human metabolome database for 2018. *Nucleic Acids Res.* **46**, D608–D617 (2018).

Acknowledgements

We thank L. Brown for providing access to the instrumentation for the lipidomics experiments. This research was supported by the Andrew Sabin Family Fellow Award and the Bridge Fund from The University of Texas MD Anderson Cancer Center (to B.G.) and grants from the National Institutes of Health (grant no. R01CA181196 to B.G.; grant nos. R35CA209896, 1R61NS109407 and P01CA087497 to B.R.S.; grant nos. R01CA166051 and R01CA181029 to L.M.). J.K.M. is supported by the Susan G. Komen PDF Basic/Translational and Clinical Funding Program (grant no. PDF17487931). T.F.W. is supported in part by the DOD (grant no. 1W81XWH-18-1-0573), the National Institutes of Health and NCI (grant no. 1R01CA215226), The Welch Foundation (grant no. Q-0007) and the McNair Medical Institute. G.R.S. is supported by a Canada Research Chair and the J. Bruce Duncan Chair in Metabolic Diseases and research grants from the Canadian Institutes of Health Research (grant no. 201709FDN-CEBA-116200) and Diabetes Canada (grant no. DI-5-17-5302-GS). B.G. is an Andrew Sabin Family Fellow. This research was also supported by the National Institutes of Health Cancer Center Support Grant P30CA016672 to The University of Texas MD Anderson Cancer Center.

Author contributions

H.L. performed most of the experiments with assistance from Y.Z., J.K.M., J.K. and L.Z. E.Z. conducted the lipidomic analysis under the direction of B.R.S. G.R.S. provided ACC DKI MEFs. D.N. provided *AMPK α 1/a2^{UL}* MEFs and the mouse model. S.T. and T.F.W. provided the inducible Cas9 vector. L.M. helped with the discussion and interpretation of results. B.G. and B.R.S. designed experiments and supervised the study. B.G. wrote most of the manuscript with assistance from H.L., F.Z. and B.R.S. All authors commented on the manuscript.

Competing interests

B.R.S. holds equity in and serves as a consultant to Inzen Therapeutics and is an inventor on patents and patent applications related to ferroptosis. The other authors declare no competing financial interests.

Additional information

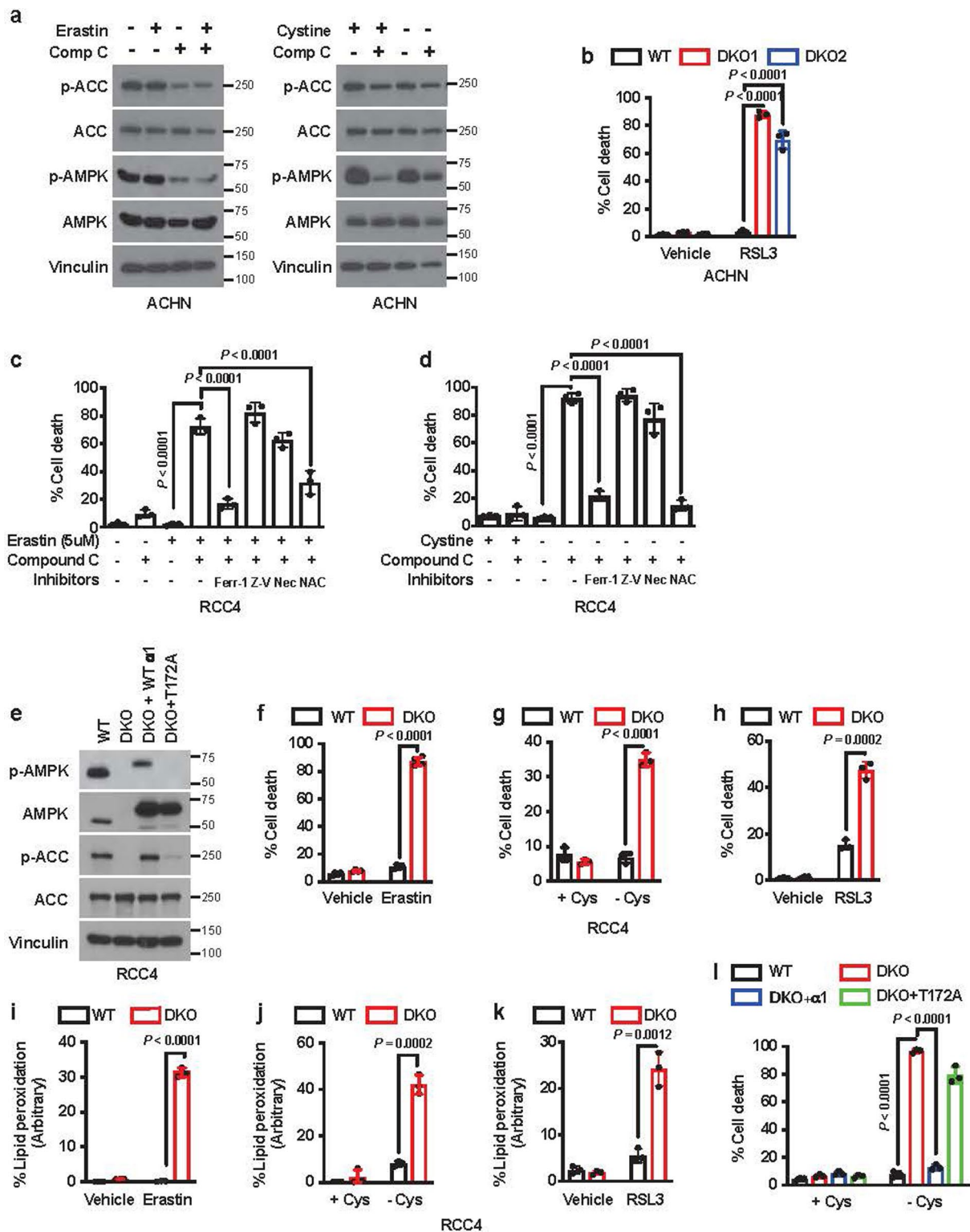
Extended data is available for this paper at <https://doi.org/10.1038/s41556-020-0461-8>.

Supplementary information is available for this paper at <https://doi.org/10.1038/s41556-020-0461-8>.

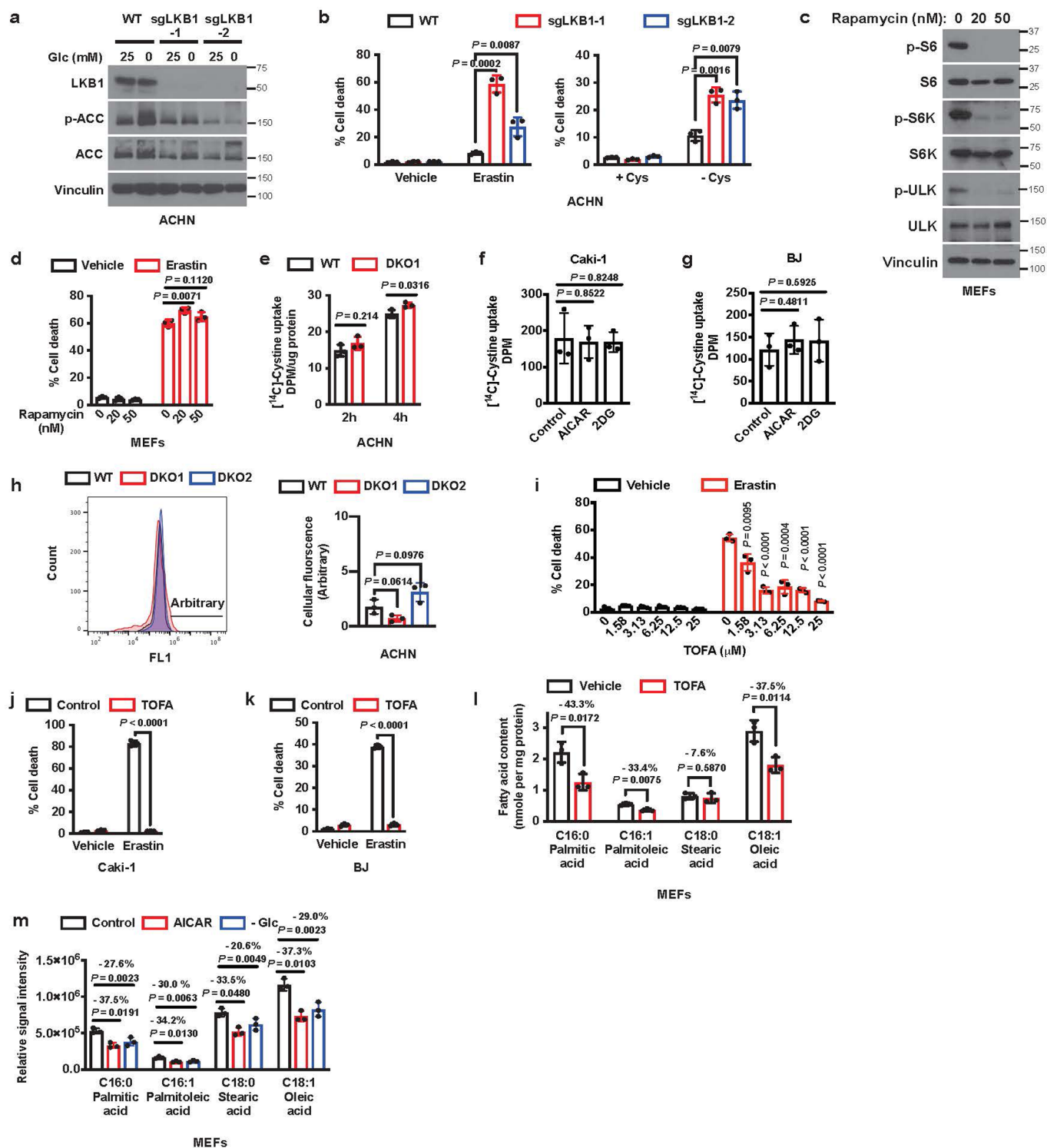
Correspondence and requests for materials should be addressed to B.R.S. or B.G.

Reprints and permissions information is available at www.nature.com/reprints.

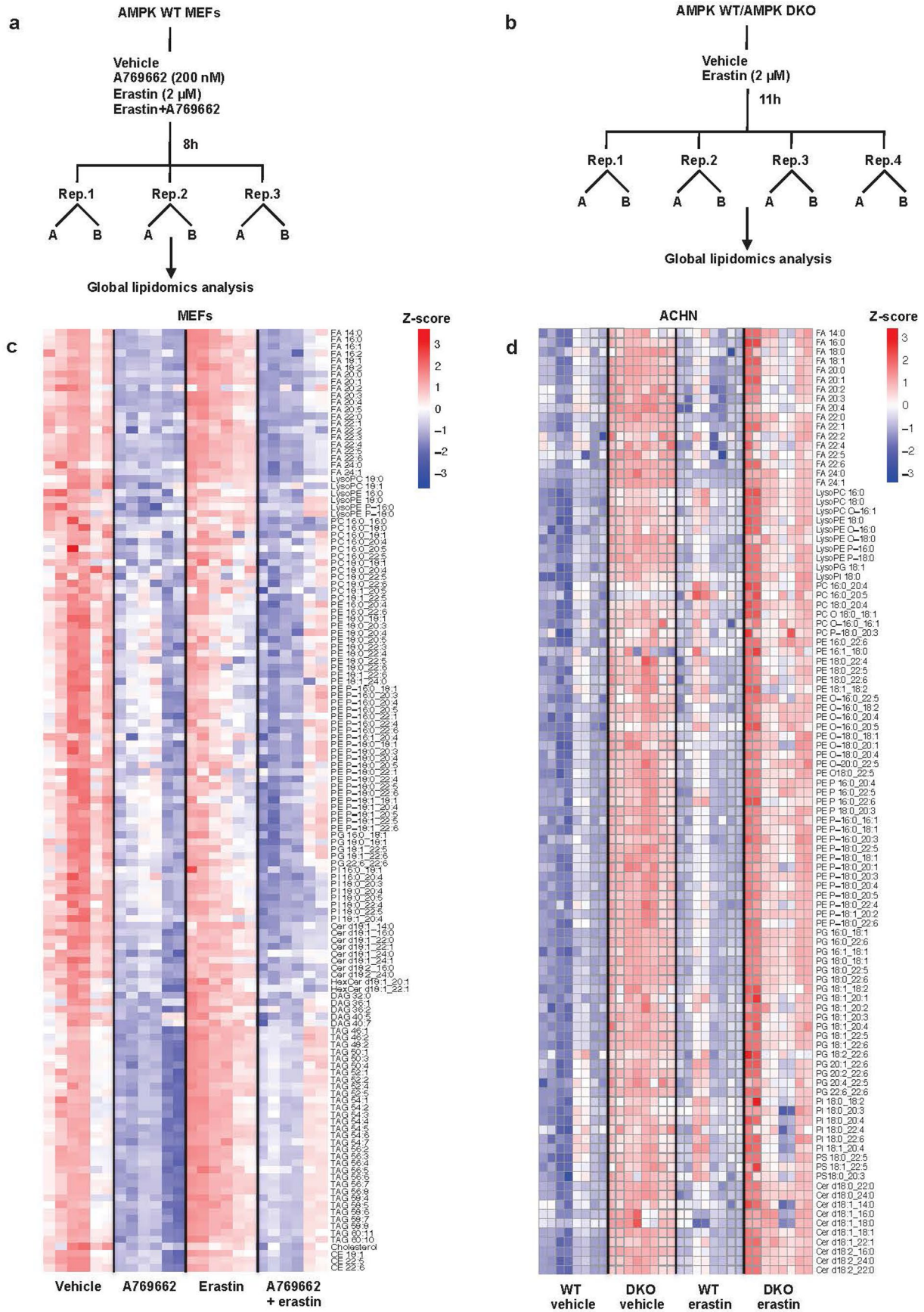
Extended Data Fig. 1 | Energy stress inhibits ferroptosis. **a**, Immunoblot analysis in MEFs treated with 2 μ M erastin (16 h), cystine free media (8 h), 100 nM RSL3 (16 h), or 1 μ M of staurosporine (STS, 2 h). **b**, Cell death measurement in MEFs treated with 2 μ M erastin and cell death inhibitors for 16 h. Ferr-1: 1 μ M ferrostatin-1; DFO: 100 μ M deferoxamine; Z-V: 20 μ M Z-VAD-FMK; Nec: 2 μ M necrostatin-1; NAC: 5 mM N-acetyl cysteine. **c**, Cell death measurement in MEFs cultured in 25 or 0 mM glucose-containing medium with erastin and/or Ferrostatin-1 for the indicated times. **d**, Immunoblot analysis in MEFs treated as in **a**, or glucose starvation for 48 h. **e**, Cell death measurement in MEFs cultured in cystine free media with cell death inhibitors for 8 h. **f, g**, Intracellular ATP levels (**f**) and cell death measurement (**g**) in MEFs cultured with the indicated concentrations of glucose for 16 h. **h-k**, The measurement of cell death (**h, j**) and lipid peroxidation (**i, k**) in Caki-1 or BJ cells. Cells were treated with A769662 (200 μ M), AICAR (2 mM), 2DG (5 mM), 0 mM glucose with simultaneous treatment of 2 μ M erastin for 24 h (cell death) and 16 h (Lipid peroxidation). *P* values correspond to the comparison between control and each treatment in red bars. **l**, Immunoblot showing the levels of AMPK T172 phosphorylation. MEFs cells were treated as in **h-k** and compound C (5 μ M) for 16 h. **m**, Cell death measurement in AMPK WT and DKO MEFs treated with 2 μ M erastin and 2 mM of AICAR for 16 h. **n**, Cell death measurement in AMPK WT and DKO MEFs treated with erastin at the indicated concentrations for 16 h. *P* values correspond to the comparison between AMPK WT and DKO at indicated erastin concentrations. Data show the mean \pm s.d., *n* = 3 independent experiments. Statistical analysis was performed using unpaired, two-tailed t-test. Numerical source data are provided in Source Data Extended Data Fig. 1. Scanned images of unprocessed blots are shown in Source Data Extended Data Fig. 1.



Extended Data Fig. 2 | AMPK inactivation renders cells sensitive to ferroptotic cell death. **a**, Western blot showing the levels of ACC (S79) and AMPK (T172) phosphorylation in ACHN cells treated with erastin for 24 h or cultured in cystine-free media for 36 h with and without compound C (10 μM). **b**, Cell death measurement in AMPK WT and DKO ACHN cell lines treated with 100 nM RSL3 for 16 h. **c**, **d**, Cell death measurement in RCC4 cells treated with 10 μM of compound C, cell death inhibitors, and 5 μM of erastin for 24 h (**c**) or in cystine free media for 36 h (**d**). Ferr-1: 1 μM ferrostatin-1; Z-V: 20 μM Z-VAD-FMK; Nec: 2 μM necrostatin-1; NAC: 5 mM N-acetyl cysteine. **e**, Western blot showing the AMPK expression in RCC4 cell as indicated. **f-h**, Cell death measurement in AMPK WT and DKO RCC4 cell lines treated with 5 μM of erastin for 24 h (**f**), cultured in cystine free media for 24 h (**g**), or treated with 100 nM of RSL3 for 24 h (**h**). **i-k**, Lipid peroxidation measurement in AMPK WT and DKO RCC4 cells treated with 5 μM of erastin for 18 h (**i**), cultured in cystine free media for 18 h (**j**), or treated with 100 nM of RSL3 for 12 h (**k**). **l**, Cell death measurement in indicated RCC4 cells cultured with cystine free media for 24 h. Data show the mean ± s.d., n = 3 independent experiments. Statistical analysis was performed using unpaired, two-tailed t-test. Numerical source data are provided in Source Data Extended Data Fig. 2. Scanned images of unprocessed blots are shown in Source Data Extended Data Fig. 2.

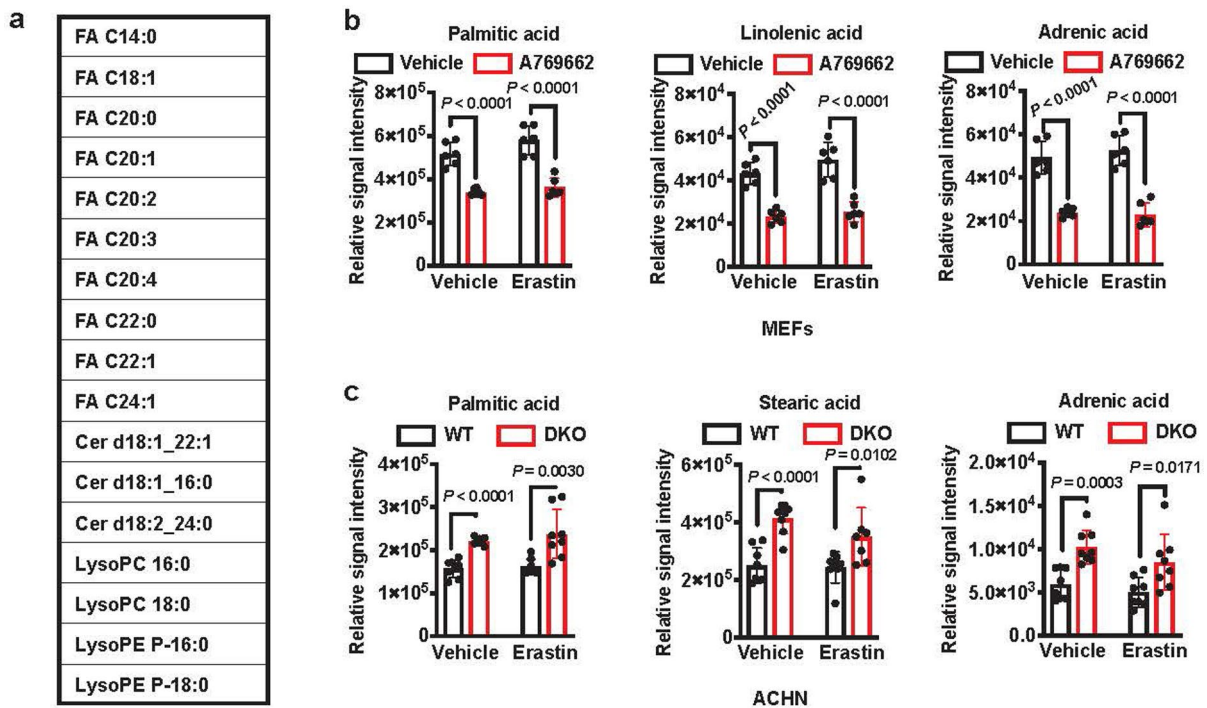


Extended Data Fig. 3 | AMPK regulates ferroptosis partly through AMPK-mediated phosphorylation of ACC. **a**, Immunoblot blot indicating the loss of LKB1 in *LKB1* KO ACHN cells generated using CRISPR/CAS9 system. **b**, Cell death in *LKB1* WT and KO ACHN cells treated with 2 μM of erastin for 24 h and cultured in cystine free media for 24 h. **c**, Immunoblot blot showing mTOR inhibition in MEFs treated with rapamycin for 8 h. **d**, Cell death in MEFs treated with 2 μM of erastin and rapamycin for 16 h. **e**, The measurement of L-[14C] Cystine uptake in AMPK WT and DKO ACHN cells. **f, g**, The measurement of L-[14C] Cystine uptake in Caki-1 (**f**) and BJ (**g**) cells treated with 2 mM AICAR and 5 mM 2DG for 6 h. **h**, The histograms and bar graphs showing the levels of intracellular labile iron in AMPK WT and DKO ACHN cells. **i**, Cell death measurement in MEFs treated with different TOFA concentrations and 2 μM erastin. *P* values correspond to the comparison between 0 μM and different concentrations of TOFA under erastin treatment. **j, k**, Cell death measurement in Caki-1 (**j**) and BJ (**k**) cells treated with 2 μM erastin and 50 μM TOFA for 24 h. **l, m**, The intracellular levels of the indicated free fatty acids in MEFs treated with vehicle or 25 μM of TOFA for 8 h (**l**) and treated with vehicle, 2 mM AICAR, or 0 mM glucose for 8 h (**m**). Data show the mean ± s.d., *n* = 3 independent experiments. Statistical analysis was performed using unpaired, two-tailed t-test. Numerical source data are provided in Source Data Extended Data Fig. 3. Scanned images of unprocessed blots are shown in Source Data Extended Data Fig. 3.

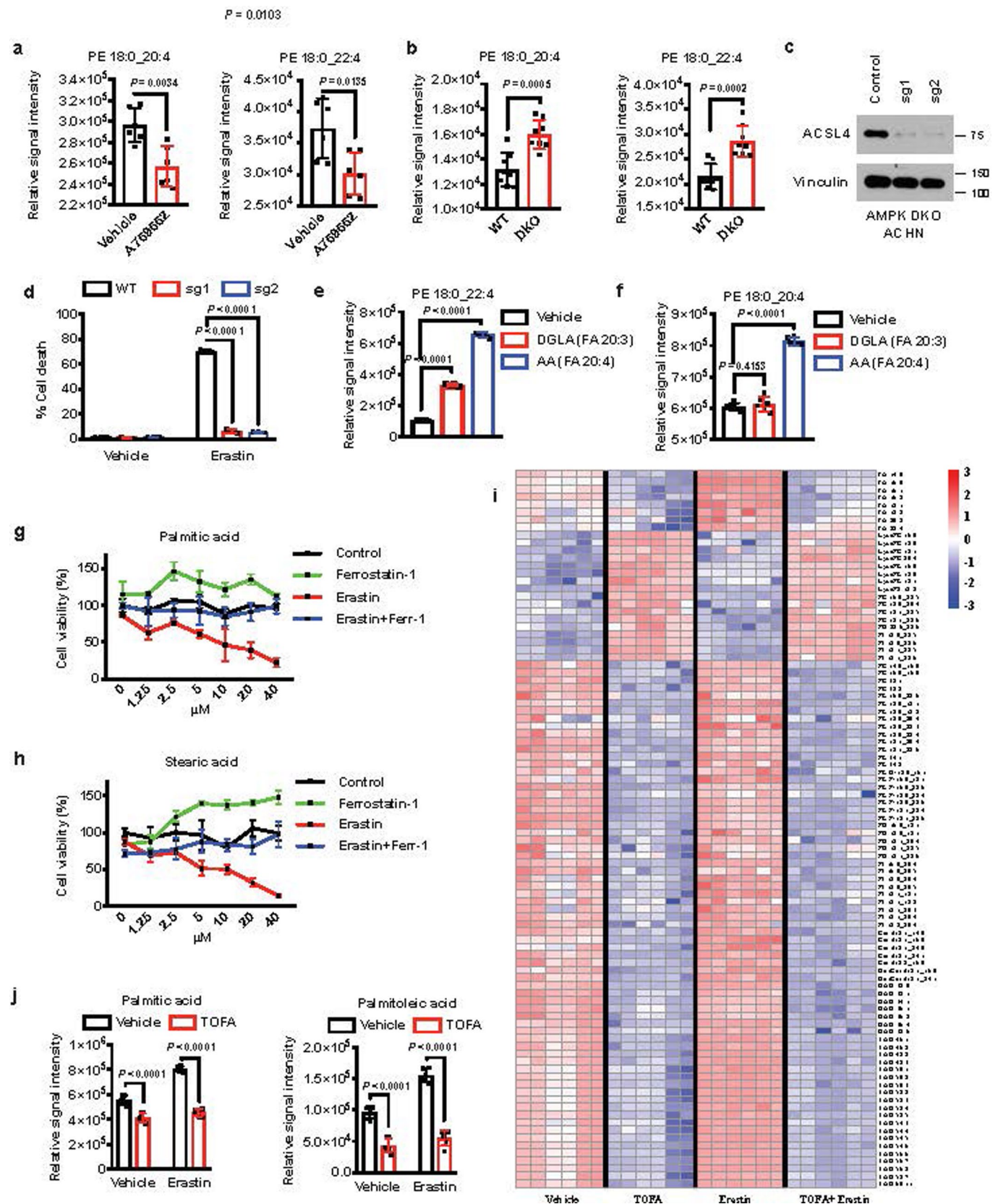


Extended Data Fig. 4 | See next page for caption.

Extended Data Fig. 4 | Lipidomic analyses upon AMPK activation or inactivation. a, b, Schematic diagram of the experimental design of mass spectrometry-based lipidomic analysis associated with AMPK activation. Global lipidomic analysis was performed in MEFs treated with vehicle, 2 μ M erastin, 200 μ M A769662, or 2 μ M erastin + 200 μ M A769662 for 8 h (**a**) or in AMPK WT and DKO ACHN cells treated with vehicle or 2 μ M erastin for 11 h (**b**). There are three biologically independent samples (Rep. 1–3) in each group (**a**) and four biologically independent samples (Rep. 1–4) in each group (**b**). Samples ran in duplicates (two technical replicates: A, B) on the UPLC-MS. **c, d**, Heat map of significantly changed lipid species (One-way ANOVA, FDR corrected p -value < 0.05) in MEFs treated with vehicle, 2 μ M erastin, 200 μ M A769662, or 2 μ M erastin + 200 μ M A769662 (**c**) or in AMPK WT and DKO ACHN cells treated with vehicle or 2 μ M erastin (**d**) combined in both positive and negative ionization modes. Each row represents z-score-normalized intensities of the detected lipid species. Each column represents a sample. The relative abundance of each lipid is color-coded with red indicating high signal intensity and blue indicating low signal intensity. (FA, free fatty acid; Cer, ceramide; PC, phosphatidylcholine; LysoPC, lysophosphatidylcholine; PC O, ether-linked PC; PC P, plasmalogen PC; LysoPC O, ether-linked LysoPC; PE, phosphatidylethanolamine; LysoPE, lysophosphatidylethanolamine; PE O, ether-linked PE; PE P, plasmalogen PE; LysoPE O, ether-linked LysoPE; LysoPE P, plasmalogen LysoPE P; PG, phosphatidylglycerol; LysoPG, lyso phosphatidylglycerol; PI, phosphatidylinositol; LysoPI, lyso phosphatidylinositol; PA, phosphatidic acid; PS, phosphatidylserine; TAG, triacylglycerol; CE, cholesteryl ester. Lipids are annotated based on the fatty acyl compositions (for example LysoPC 16:0, 16 carbons and 0 double bond) or as sum of total number of carbons and double bonds (for example TAG 52:5, total of 52 carbons and 5 double bonds).

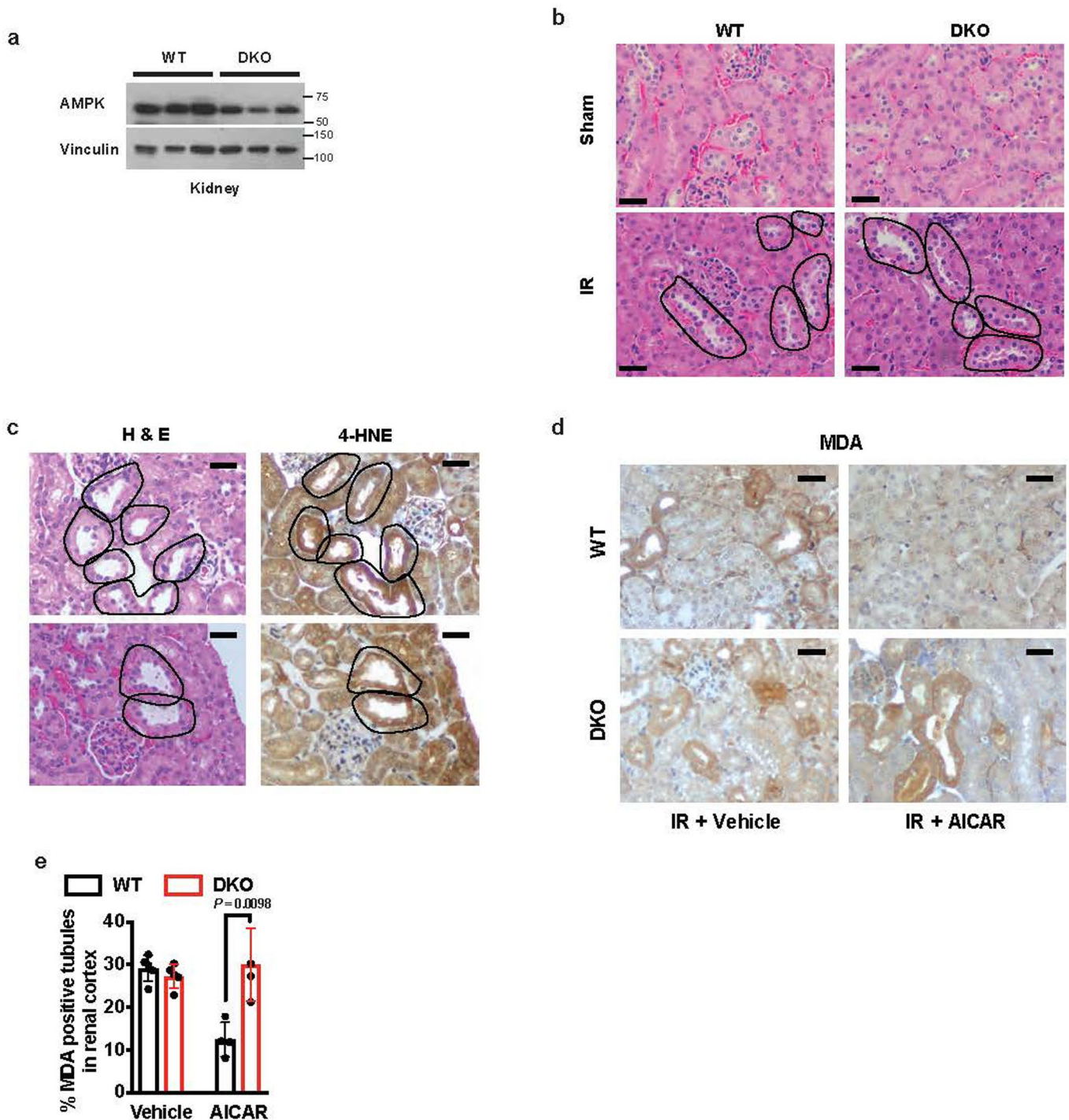


Extended Data Fig. 5 | The levels of fatty acids were altered by AMPK activation or inactivation. **a**, List of 17 lipid species significantly changed (Two-tailed, unpaired Welch's t-test, Fold change ≥ 1.5 and FDR-corrected p -value < 0.05) in both MEFs (vehicle versus A769662) and ACHN (AMPK WT versus DKO) cells. Refer to Extended Data Fig. 4 for detailed sample information. **b, c**, The relative signal intensities of the indicated free fatty acids involved in long chain fatty acid biosynthesis in MEFs (**b**) or ACHN (**c**) cells with the indicated treatment and genotypes. Data show the mean \pm s.d., $n = 6$ (**b**) or $n = 8$ (**c**) independent experiments. Statistical analysis was performed using unpaired, two-tailed t-test. Numerical source data are provided in Source Data Extended Data Fig. 5.

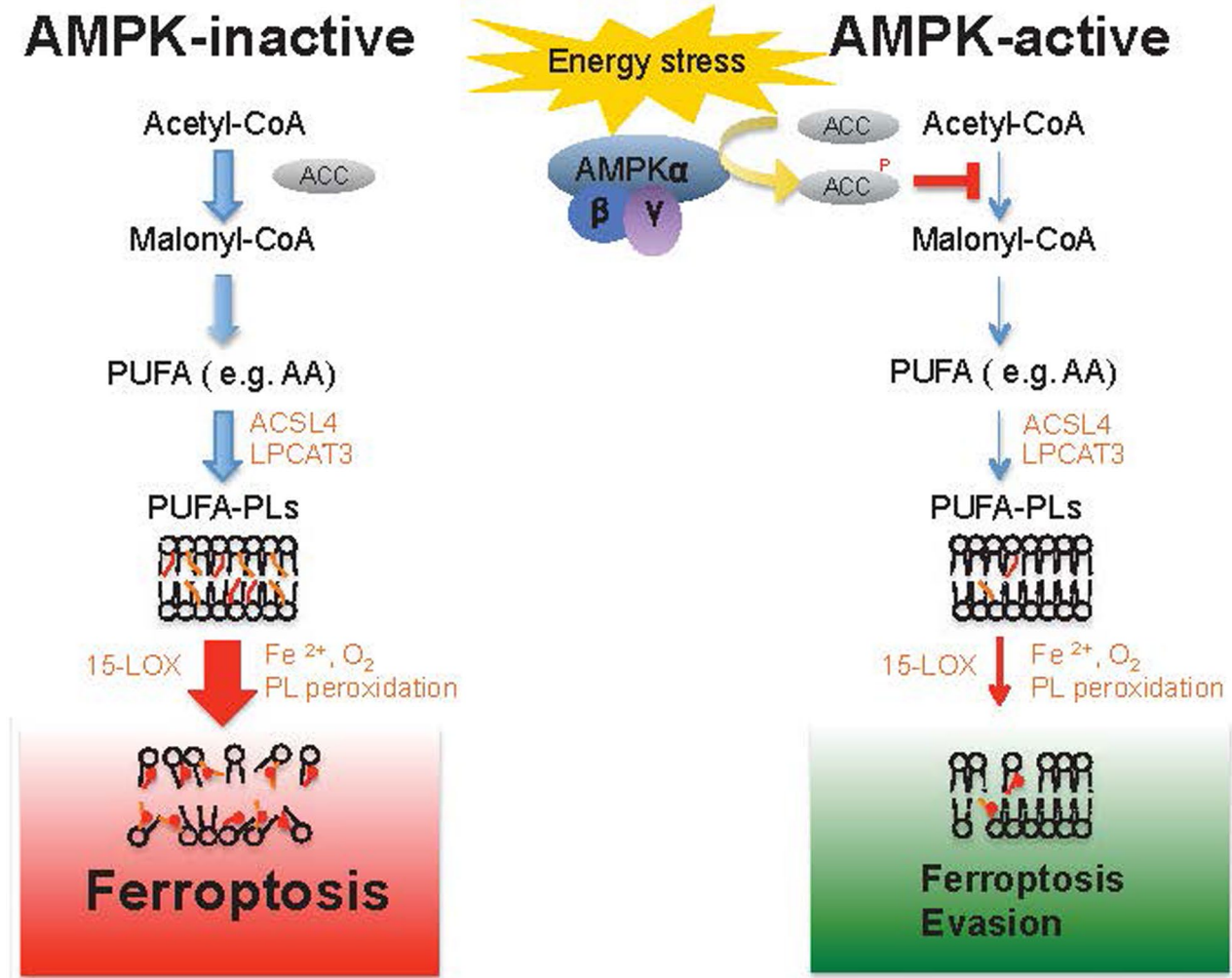


Extended Data Fig. 6 | See next page for caption.

Extended Data Fig. 6 | AMPK activation suppresses PUFA biosynthesis. a, b, The relative signal intensities of PE 18:0_20:4 and PE 18:0_22:4 in MEFs treated with A769662 (**a**) or *AMPK* WT and DKO ACHN cells (**b**). **c**, Immunoblot indicating the loss of *ACSL4* in *AMPK* DKO ACHN cells. The experiment was repeated twice, independently, with similar results. **d**, Cell death in *AMPK* DKO ACHN cells with *ACSL4* WT and KO upon treatment of 2 μ M erastin. **e, f**, The relative signal intensities of PE 18:0_22:4 (**e**) and PE 18:0_20:4 (**f**) in ACHN cells treated with 20 μ M dihomo- γ -linolenic acid or arachidonic acid for 42 h. **g, h**, Cell viability measurement in ACHN cells incubated with palmitic acid (**g**) or stearic acid (**h**) with a series of concentration (0 μ M-40 μ M) and treated with or without ferrostatin-1 (Ferr-1) or erastin as indicated. **i**, Heat map of significantly changed lipid species (One-way ANOVA, FDR corrected p -value < 0.05) in MEFs treated with vehicle, 25 μ M TOFA, 2 μ M erastin, or 25 μ M TOFA + 2 μ M erastin combined positive and negative ionization modes. There are three biologically independent samples in each group and the samples analyzed in duplicates (technical replicates) on the UPLC-MS. Each row represents z-score-normalized relative signal intensities of the identified lipid species. Each column represents a sample. The relative abundance of each lipid is color-coded with red indicating high signal intensity and blue indicating low signal intensity. **j**, The relative signal intensities of the indicated fatty acids in MEFs treated with vehicle or 25 μ M TOFA. Data show the mean \pm s.d., $n=3$ (**d, g, h**), $n=6$ (**a, e, f, j**) or $n=8$ (**b**) independent experiments. Statistical analysis was performed using unpaired, two-tailed t-test. Scanned images of unprocessed blots are shown in Source Data Extended Data Fig. 6. Numerical source data are provided in Source Data Extended Data Fig. 6.



Extended Data Fig. 8 | Renal ischemia reperfusion injury in $AMPK\ \alpha1/\alpha2^{L/L}$ or $AMPK\alpha1/\alpha2^{L/L}, Rosa26-CreERT2$ mice. **a**, Immunoblot showing the levels of AMPK α expression in kidneys of three individual $AMPK\ \alpha1/\alpha2^{L/L}$ or $AMPK\alpha1/\alpha2^{L/L}, Rosa26-CreERT2$ mice (referred to as AMPK WT and KO mice). The experiment was repeated three times, independently, with similar results. **b**, Representative images of hematoxylin and eosin (H&E) staining of the renal cortex in sham-treated and IR-operated AMPK WT or DKO mice. Damaged renal tubules are marked by black dotted lines. Scale bars, 50 μ m. The experiment was repeated more than ten times, independently, with similar results. **c**, Representative images of H&E staining and immunohistochemical staining of 4-HNE from mouse renal cortex after IR. Damaged renal tubules are marked with black dotted lines and 4-HNE stained tubules are marked with red dotted lines. Scale bars, 50 μ m. The experiment was repeated more than ten times, independently, with similar results. **d, e**, Representative images showing MDA immunohistochemical staining from mouse renal cortex with the indicated genotypes and treatment conditions (**d**; dark brown stained tubules indicate MDA positive staining, Scale bars, 50 μ m). Bar graphs presenting the percentages of MDA positive tubules per visual field (**e**). Data show the mean \pm s.d., $n=4$ (AICAR) or $n=5$ (vehicle) independent experiments. Statistical analysis was performed using unpaired, two-tailed t-test. Scanned images of unprocessed blots are shown in Source Data Extended Data Fig. 8. Numerical source data are provided in Source Data Extended Data Fig. 8.



Extended Data Fig. 9 | A schematic model describing the roles of AMPK-mediated energy stress signaling in regulating ferroptosis. See discussion for the detailed description. ACC: acetyl-CoA carboxylase; PUFAs: polyunsaturated fatty acids; AA: arachidonic acid; PUFA-PLs: polyunsaturated fatty acid-containing phospholipids; ACSL4: acyl-CoA synthetase long chain family member 4; LPCAT3: lysophosphatidylcholine acyltransferase 3; 15-LOX: 15-lipoxygenase.

Reporting Summary

Nature Research wishes to improve the reproducibility of the work that we publish. This form provides structure for consistency and transparency in reporting. For further information on Nature Research policies, see [Authors & Referees](#) and the [Editorial Policy Checklist](#).

Statistics

For all statistical analyses, confirm that the following items are present in the figure legend, table legend, main text, or Methods section.

- | n/a | Confirmed |
|-------------------------------------|--|
| <input type="checkbox"/> | <input checked="" type="checkbox"/> The exact sample size (n) for each experimental group/condition, given as a discrete number and unit of measurement |
| <input type="checkbox"/> | <input checked="" type="checkbox"/> A statement on whether measurements were taken from distinct samples or whether the same sample was measured repeatedly |
| <input type="checkbox"/> | <input checked="" type="checkbox"/> The statistical test(s) used AND whether they are one- or two-sided
<i>Only common tests should be described solely by name; describe more complex techniques in the Methods section.</i> |
| <input checked="" type="checkbox"/> | <input type="checkbox"/> A description of all covariates tested |
| <input checked="" type="checkbox"/> | <input type="checkbox"/> A description of any assumptions or corrections, such as tests of normality and adjustment for multiple comparisons |
| <input type="checkbox"/> | <input checked="" type="checkbox"/> A full description of the statistical parameters including central tendency (e.g. means) or other basic estimates (e.g. regression coefficient) AND variation (e.g. standard deviation) or associated estimates of uncertainty (e.g. confidence intervals) |
| <input type="checkbox"/> | <input checked="" type="checkbox"/> For null hypothesis testing, the test statistic (e.g. F , t , r) with confidence intervals, effect sizes, degrees of freedom and P value noted
<i>Give P values as exact values whenever suitable.</i> |
| <input checked="" type="checkbox"/> | <input type="checkbox"/> For Bayesian analysis, information on the choice of priors and Markov chain Monte Carlo settings |
| <input checked="" type="checkbox"/> | <input type="checkbox"/> For hierarchical and complex designs, identification of the appropriate level for tests and full reporting of outcomes |
| <input checked="" type="checkbox"/> | <input type="checkbox"/> Estimates of effect sizes (e.g. Cohen's d , Pearson's r), indicating how they were calculated |

Our web collection on [statistics for biologists](#) contains articles on many of the points above.

Software and code

Policy information about [availability of computer code](#)

Data collection

Accuri C6 (BS Bioscience) was used to collect flow cytometry data; MassLynx 4.1 was used for LC-MS data acquisition

Data analysis

Graphpad Prism 8 was used for bar graphs output and statistic analysis; FlowJo10 was used for flow cytometry data analysis; Image J was used for histological image analysis; XCMS package 3.0.2 and R 3.4.4 were used for extracting lipid features and data processing; MetaboAnalyst 4.0 and Venny 2.1.0 were used for lipidomic data comparisons and statistics analyses.

For manuscripts utilizing custom algorithms or software that are central to the research but not yet described in published literature, software must be made available to editors/reviewers. We strongly encourage code deposition in a community repository (e.g. GitHub). See the Nature Research [guidelines for submitting code & software](#) for further information.

Data

Policy information about [availability of data](#)

All manuscripts must include a [data availability statement](#). This statement should provide the following information, where applicable:

- Accession codes, unique identifiers, or web links for publicly available datasets
- A list of figures that have associated raw data
- A description of any restrictions on data availability

Raw mass spectrometry data files, processed data, and annotated lipid features are available in EMBL-EBI MetaboLights database (reference: PMID: 23109552) with the identifier MTBLS1399 (<https://www.ebi.ac.uk/metabolights/MTBLS1399>)

Field-specific reporting

Please select the one below that is the best fit for your research. If you are not sure, read the appropriate sections before making your selection.

- Life sciences Behavioural & social sciences Ecological, evolutionary & environmental sciences

For a reference copy of the document with all sections, see [nature.com/documents/nr-reporting-summary-flat.pdf](https://www.nature.com/documents/nr-reporting-summary-flat.pdf)

Life sciences study design

All studies must disclose on these points even when the disclosure is negative.

Sample size	No sample size calculations were performed. Sample size was determined according to our experience as well as literature reporting in terms of specific experiment.
Data exclusions	No data were excluded from the data analyses.
Replication	Multiple independent repeats were included for related experiments. Each experiment was performed for at least twice to make sure similar results are reproducible. Mass spectrometry-based lipidomics experiments have been done in two technical replicates with three (Fig. 5a, Extended Data Fig. 4c, Extended Data Fig. 6i) or four (Fig. 5b, Extended Data Fig. 4d) independent biological replicates in each group.
Randomization	7-8 weeks old wild-type mice were used for ischemia/reperfusion injury experiments, and randomly allocated into experimental groups.
Blinding	For cell-based experiments, EM, Western blotting, immunostaining and FACS, cell types were known when prepare the samples or start to treat cells at the beginning of experiments. Data measurement for cell viability and FACS, photo capture or histological analysis were blinded to different person who processed assay at the time.

Reporting for specific materials, systems and methods

We require information from authors about some types of materials, experimental systems and methods used in many studies. Here, indicate whether each material, system or method listed is relevant to your study. If you are not sure if a list item applies to your research, read the appropriate section before selecting a response.

Materials & experimental systems

n/a	Involved in the study
<input type="checkbox"/>	<input checked="" type="checkbox"/> Antibodies
<input type="checkbox"/>	<input checked="" type="checkbox"/> Eukaryotic cell lines
<input checked="" type="checkbox"/>	<input type="checkbox"/> Palaeontology
<input type="checkbox"/>	<input checked="" type="checkbox"/> Animals and other organisms
<input checked="" type="checkbox"/>	<input type="checkbox"/> Human research participants
<input checked="" type="checkbox"/>	<input type="checkbox"/> Clinical data

Methods

n/a	Involved in the study
<input checked="" type="checkbox"/>	<input type="checkbox"/> ChIP-seq
<input type="checkbox"/>	<input checked="" type="checkbox"/> Flow cytometry
<input checked="" type="checkbox"/>	<input type="checkbox"/> MRI-based neuroimaging

Antibodies

Antibodies used

phospho-AMPK α (Thr172, 1:1000, 2535, Cell Signaling), AMPK α (1:1000, 5832, Cell Signaling) AMPK α 1 (1:1000, 2795, Cell Signaling), AMPK α 2 (1:1000, 2757, Cell Signaling), phospho-ACC (S79, 3661, 1:1000, Cell Signaling), ACC (1:1000, 3662, Cell Signaling), phospho-S6 (Ser240/244, 1:5000, 3661, Cell Signaling), S6 (1:1000, 2217, Cell Signaling), phospho-S6K (Thr389, 1:1000, 9205, Cell Signaling), S6K (1:1000, sc-230, Santa Cruz), phospho-ULK1 (S757, 6888, 1:1000, Cell Signaling), ULK1 (1:1000, 8054, Cell Signaling), LKB1 (1:1000, sc-32245, Santa Cruz), SLC7A11 (1:3000, 12691, Cell Signaling), GPX4 (1:1000, MAB5457, R&D systems), ACSL4 (1:1000, sc-271800, Santa Cruz), Cleaved Caspase-3 (Asp175, 1:500, 9661, Cell Signaling), Cleaved-PARP (Asp214, 1:1000, 9544, Cell Signaling), Vinculin (1:50000, V4505, Sigma).

Validation

All antibodies used in our study have been validated and detailed information could be found on the website from manufactures as listed below.
 phospho-AMPK α , <https://www.cellsignal.com/products/primary-antibodies/phospho-ampka-thr172-40h9-rabbit-mab/2535>;
 AMPK α , <https://www.cellsignal.com/products/primary-antibodies/ampka-d63g4-rabbit-mab/5832>; AMPK α 1, <https://www.cellsignal.com/products/primary-antibodies/ampka1-antibody/2795>; AMPK α 2, <https://www.cellsignal.com/products/primary-antibodies/ampka2-antibody/2757>; phospho-ACC, <https://www.cellsignal.com/products/primary-antibodies/phospho-acetyl-coa-carboxylase-ser79-antibody/3661>; ACC, <https://www.cellsignal.com/products/primary-antibodies/acetyl-coa-carboxylase-antibody/3662>; phospho-S6, <https://www.cellsignal.com/products/primary-antibodies/phospho-s6-ribosomal-protein-ser240-244-antibody/2215>; S6, <https://www.cellsignal.com/products/primary-antibodies/s6-ribosomal-protein-5g10-rabbit-mab/2217>; phospho-S6K, <https://www.cellsignal.com/products/primary-antibodies/phospho-p70-s6-kinase-thr389-antibody/9205>; S6K, <https://www.scbt.com/scbt/product/p70-s6-kinase-alpha-antibody-h-9>; phospho-ULK1, <https://www.cellsignal.com/products/primary-antibodies/phospho-ulk1-ser757-antibody/6888>; ULK1, <https://www.cellsignal.com/products/primary-antibodies/ulk1-d8h5-rabbit-mab/8054>; LKB1, <https://www.scbt.com/scbt/product/lkb1-antibody-ley-37d>

g6requestFrom=search; SLC7A11 <https://www.cellsignal.com/products/primary-antibodies/xct-slc7a11-d2m7a-rabbit-mab/12691>; GPX4, https://www.rndsystems.com/products/human-mouse-rat-glutathione-peroxidase-4-gpx4-antibody-565320_mab5457; ACSL4, <https://www.scbt.com/scbt/product/acsl4-antibody-a-5>; Cleaved Caspase-3, <https://www.cellsignal.com/products/primary-antibodies/cleaved-caspase-3-asp175-antibody/9661>; Cleaved-PARP, <https://www.cellsignal.com/products/primary-antibodies/cleaved-parp-asp214-antibody-mouse-specific/9544>; Vinculin, <https://www.sigmaaldrich.com/catalog/product/sigma/v4505?lang=en®ion=US>

Eukaryotic cell lines

Policy information about [cell lines](#)

Cell line source(s)	BJ, ACHN, Caki-1, A498, MCF7, MDA-MB-231, A375, and A549 cell lines were obtained from ATCC. RCC4 and UMRC6 cell lines were obtained from Dr. William G. Kaelin at Dana-Farber Cancer Institute. PANC-1 and DanG cell lines were obtained from Dr. Haoqiang Ying at MD Anderson Cancer Center. H157 cell line was obtained from Dr. Jack A. Roth at MD Anderson Cancer Center. Primary mouse embryonic fibroblasts (MEFs) were established from embryos at E13.5 and immortalized by infection of SV40 large T antigen.
Authentication	Cell lines were not authenticated.
Mycoplasma contamination	All cell lines tested negative for mycoplasma contamination.
Commonly misidentified lines (See ICLAC register)	No ICLAC cell lines were used in this study

Animals and other organisms

Policy information about [studies involving animals](#); [ARRIVE guidelines](#) recommended for reporting animal research

Laboratory animals	7-8 weeks old female C57BL/6J mice were purchased from ERO mouse facility in MD anderson cancer center. AMPK α 1/ α 2 floxed mice were provided by Dr. Daisuke Nakada (Saito et al., 2015) and crossed with Rosa26-CreERT2 (The Jackson Laboratory, Stock No. 008463) mice. Mice were C57BL/6 background. Both female and male mice were injected with tamoxifen at 5 weeks old and subjected to ischemia/reperfusion at 2 weeks post tamoxifen injection.
Wild animals	No wild animal was used in this study.
Field-collected samples	No sample collected from field was used in this study.
Ethics oversight	All the animal experiments were performed in accordance with a protocol approved by the Institutional Animal Care and Use Committee and Institutional Review Board at The University of Texas MD Anderson Cancer Center.

Note that full information on the approval of the study protocol must also be provided in the manuscript.

Flow Cytometry

Plots

Confirm that:

- The axis labels state the marker and fluorochrome used (e.g. CD4-FITC).
- The axis scales are clearly visible. Include numbers along axes only for bottom left plot of group (a 'group' is an analysis of identical markers).
- All plots are contour plots with outliers or pseudocolor plots.
- A numerical value for number of cells or percentage (with statistics) is provided.

Methodology

Sample preparation	For lipid peroxidation, cultured cells were collected from 12-well plates and incubated with 5 μ M BODIPYTM 581/591 C11 dye (Invitrogen, D3861) for 30 min at 37°C in a water bath. Then cells were subjected to flow cytometry analysis by BD Accuri C6 using a 488 nm laser on a FL1 detector. For cell death analysis, collected cells were stained with 5 μ g/ml of propidium iodide (PI) and the percentage of PI-positive dead cell population was analyzed by the flow cytometer, BD Accuri C6 (BD Biosciences) using a FL2 detector.
Instrument	Accuri C6 (BD biosciences)
Software	Accuri C6 software was used for data collection and FlowJo_V10 software was used for data analysis.
Cell population abundance	Minimum of 5,000 single cells were analyzed for data collection.

Gating strategy

Initial cell population gating (FSC-Area VS FSC-Height) was adopted to make sure doublet exclusion and only single cell was used for analysis. An identical cell gating strategy was applied to all samples analyzed at the same time.

Tick this box to confirm that a figure exemplifying the gating strategy is provided in the Supplementary Information.